A&A 555, A68 (2013)
DOI: 10.1051/0004-6361/201321351

Astronomy & Astrophysics

The UVES Large Program for testing fundamental physics I. Bounds on a change in α towards quasar HE 2217−2818⋆,⋆⋆

P. Molaro[1,7], M. Centurión[1], J. B. Whitmore[2], T. M. Evans[2], M. T. Murphy[2], I. I. Agafonova[3], P. Bonifacio[4], S. D'Odorico[5], S. A. Levshakov[3,12], S. Lopez[6], C. J. A. P. Martins[7], P. Petitjean[8], H. Rahmani[10], D. Reimers[9], R. Srianand[10], G. Vladilo[1], and M. Wendt[11,9]

[1] INAF−Osservatorio Astronomico di Trieste, via G. B. Tiepolo 11, 34131 Trieste, Italy
e-mail: molaro@oats.inaf.it
[2] Centre for Astrophysics and Supercomputing, Swinburne University of Technology, Hawthorn, VIC 3122, Australia
[3] Ioffe Physical-Technical Institute, Polytekhnicheskaya, Str. 26, 194021 Saint Petersburg, Russia
[4] GEPI, Observatoire de Paris, CNRS, Univ. Paris Diderot, Place Jules Janssen, 92190 Meudon, France
[5] ESO, Karl-Schwarzschild-Str. 1, 85741 Garching, Germany
[6] Departamento de Astronomia, Universidad de Chile, Casilla 36-D, Santiago, Chile
[7] Centro de Astrofísica, Universidade do Porto, Rua das Estrelas, 4150-762 Porto, Portugal
[8] Université Paris 6, Institut d'Astrophysique de Paris, CNRS UMR 7095, 98bis bd Arago, 75014 Paris, France
[9] Hamburger Sternwarte, Universität Hamburg, Gojenbergsweg 112, 21029 Hamburg, Germany
[10] Inter-University Centre for Astronomy and Astrophysics, Post Bag 4, Ganeshkhind, 411 007 Pune, India
[11] Institut für Physik und Astronomie, Universität Potsdam, 14476 Golm, Germany
[12] St. Petersburg Electrotechnical University "LETI", Prof. Popov Str. 5, 197376 St. Petersburg, Russia

Received 22 February 2013 / Accepted 3 May 2013

ABSTRACT

Context. Absorption-line systems detected in quasar spectra can be used to compare the value of the fine-structure constant, α, measured today on Earth with its value in distant galaxies. In recent years, some evidence has emerged of small temporal and also spatial variations in α on cosmological scales. These variations may reach a fractional level of ≈10 ppm (parts per million).
Aims. To test these claims we are conducting a Large Program of observations with the Very Large Telescope's Ultraviolet and Visual Echelle Spectrograph (UVES), and are obtaining high-resolution ($R \approx 60\,000$) and high signal-to-noise ratio ($S/N \approx 100$) UVES spectra calibrated specifically for this purpose. Here we analyse the first complete quasar spectrum from this programme, that of HE 2217−2818.
Methods. We applied the many multiplet method to measure α in five absorption systems towards this quasar: $z_{\rm abs} = 0.7866$, 0.9424, 1.5558, 1.6279 , and 1.6919.
Results. The most precise result is obtained for the absorber at $z_{\rm abs} = 1.6919$ where 3 Fe II transitions and Al II λ1670 have high S/N and provide a wide range of sensitivities to α. The absorption profile is complex with several very narrow features, and it requires 32 velocity components to be fitted to the data. We also conducted a range of tests to estimate the systematic error budget. Our final result for the relative variation in α in this system is $\Delta\alpha/\alpha = +1.3 \pm 2.4_{\rm stat} \pm 1.0_{\rm sys}$ ppm. This is one of the tightest current bounds on α-variation from an individual absorber. A second, separate approach to the data reduction, calibration, and analysis of this system yielded a slightly different result of $-3.8 \pm 2.1_{\rm stat}$ ppm, possibly suggesting a larger systematic error component than our tests indicated. This approach used an additional 3 Fe II transitions, parts of which were masked due to contamination by telluric features. Restricting this analysis to the Fe II transitions alone and using a modified absorption profile model gave a result that is consistent with the first approach, $\Delta\alpha/\alpha = +1.1 \pm 2.6_{\rm stat}$ ppm. The four other absorbers have simpler absorption profiles, with fewer and broader features, and offer transitions with a narrower range of sensitivities to α. They therefore provide looser bounds on $\Delta\alpha/\alpha$ at the ≳10 ppm precision level.
Conclusions. The absorbers towards quasar HE 2217−2818 reveal no evidence of any variation in α at the 3-ppm precision level (1σ confidence). If the recently reported 10-ppm dipolar variation in α across the sky is correct, the expectation at this sky position is (3.2−5.4) ± 1.7 ppm depending on dipole model used. Our constraint of $\Delta\alpha/\alpha = +1.3 \pm 2.4_{\rm stat} \pm 1.0_{\rm sys}$ ppm is not inconsistent with this expectation.

Key words. quasars: absorption lines – quasars: individual: HE 2217-2818 – intergalactic medium – cosmology: miscellaneous – cosmology: observations

1. Introduction

Metal lines of absorption systems due to intervening galaxies along the line of sight towards distant quasars provide insight into the atomic structure at the cosmic time and location of the intervening object. All atomic transitions depend on the fine-structure constant, offering a way to probe possible variations in its value in space and time. The seminal papers of Savedoff (1956) and Bahcall et al. (1967) took advantage of the dependence of the relative separation of fine-structure doublet transitions on α and used the alkali doublets observed in the first extragalactic sources to limit $\Delta\alpha/\alpha$ at the level of a few percent. More

⋆ Based on observations taken at ESO Paranal Observatory. Program L 185.A-0745
⋆⋆ Tables 4−8 are available in electronic form at http://www.aanda.org

recently, the many-multiplet (MM) method has been introduced, which allows all observed transitions to be compared, thereby gaining access to the typically much larger dependence of the ground-state energy levels on α (Dzuba et al. 1999). Overall, the MM method improves the sensitivity to the measurement of a variation in α by more than an order of magnitude over the alkali-doublet method. Moreover, the individual dependence on α of different atoms and transitions allows better control of instrumental and astrophysical systematic errors.

A first analysis using the MM method on quasar absorption spectra obtained at the Keck telescope revealed hints that in the early universe the fine structure constant was smaller than today by ∼6 parts per million (ppm; Webb et al. 1999; Murphy et al. 2001, 2003). However, the analysis of smaller data sets obtained from the Very Large Telescope (VLT) in Chile by other groups did not confirm the variation of α (Quast et al. 2004; Chand et al. 2004; Levshakov et al. 2005, 2006), though in some cases these analyses and uncertainty estimates have been challenged (Murphy et al. 2007b, 2008) (but see Srianand et al. 2007). A recent analysis has been performed on a new sample built up by merging 141 measurements from Keck with 154 measurements from VLT (Webb et al. 2011; King et al. 2012). The merged sample indicates a spatial variation in α across the sky at the 4.1σ level with amplitude ∼10 ppm. Since the Keck telescope in Hawaii is at a latitude of 20° N, and the VLT in Chile is at latitude of 25° S, the two subsamples survey relatively different hemispheres, and the study of the merged sample provides a much more complete sky coverage. Remarkably, the two sets of measurements are consistent along the region of the sky covered by the two telescopes. So far, this spatial variation has been formally consistent with the null results obtained by other groups since the lines-of-sight fall into a region with minimal reported variation.

It has to be noted that a large-scale spatial variation of this magnitude is not expected. It cannot be obtained easily in the simplest theoretical models where varying fundamental couplings are due to dynamical scalar fields. One can nevertheless reproduce it by constructing toy models, for example, as the result of domains formed at the spontaneous breaking of a discrete symmetry for a dilaton-like scalar field coupled to electromagnetism (Olive et al. 2011). In any case, if such a result is confirmed, it will highlight the presence of currently unknown mechanisms that cause nature's physical couplings to have different values in different regions of the universe. Observational and experimental confirmation or refutation of these results is therefore important. In addition to their intrinsic interest, these measurements (either detections or null results) can shed light on the enigma of dark energy (Amendola et al. 2012).

One possible weakness in the evidence for variations in α is that it derives mostly from archival Keck and VLT spectra. In particular, the majority of the spectra analysed by King et al. (2012) were obtained in service observing mode at the VLT. While spectroscopic quasar observations are generally straightforward, the service calibration plan for most VLT/UVES observations only include wavelength calibration exposures of a thorium-argon (ThAr) lamp many hours after the relevant quasar exposures. This introduces the possibility of systematic miscalibrations of the quasar wavelength scales. With this possibility in mind, and motivated by the need to confirm or refute current evidence for variations in α, we are conducting ESO Large Program 185.A-0745, "The UVES Large Program for testing Fundamental Physics". The aim is to obtain high signal-to-noise ratio ($S/N \sim 100$ per pixel) spectra of ∼12 bright quasars, carefully selected to contain a total of ∼25 absorbers along their sight lines in which $\Delta\alpha/\alpha$ can be determined with precision better than ∼10 ppm. In each quasar line-of-sight there is at least one absorber in which we expect a precision approaching ∼2 ppm based on the variety of metal-line transitions available and the shape/structure of their absorption profiles.

In the present work we focus on the first line-of-sight from the programme: the bright quasar HE 2217−2818. This sight line shows five separate absorption systems at redshifts 0.9−1.7 in which α-sensitive transitions can be observed at high resolution with unusually high S/N. This line of sight subtends an angle of $\Theta \approx 58°$ with respect to the pole of the simplest model of dipolar variation in α across the sky in King et al. (2012). The expected signal at this position on the sky is therefore $\Delta\alpha/\alpha \approx +5.4$ ppm. Achieving a statistical precision in $\Delta\alpha/\alpha$ of $\lesssim$2 ppm as we aim to do in the $z_{\rm abs} = 1.6919$ absorber towards HE 2217−2818 in this paper using our new, high-S/N observations therefore contains the possibility of evidence for or against the dipolar model of spatial variation in α. However, another major goal of studying this first quasar from the Large Program is to reveal systematic errors that may not randomize over the larger sample we will present in future papers. In particular, for the absorption system at $z_{\rm abs} = 1.6919$, we present the results of two separate analyses to assist in the assessment of systematic effects.

2. Data analysis

2.1. Observations

HE 2217−2818 is a relatively bright quasar with $V \approx 16.0$ and with $z_{\rm em} = 2.46$. Its spectrum shows several intervening systems at $z_{\rm abs} = 0.600$, 0.7866, 0.9424, 1.054, 1.083, 1.200, 1.5558, 1.6279, 1.6919 , and 2.181. However, only some of them, i.e. those detected in multiple transitions of the low-ionization ions Fe II, Si II, and Mg II at $z_{\rm abs}$= 0.7866, 0.9424, 1.5558, 1.6279, and 1.6919, are suitable for probing the fine-structure constant. The other systems have metal lines that are either too weak or which fall in the Lyman forest shortwards of ≈420 nm.

The observations of HE 2217−2818 were performed with UVES on VLT on the nights of 13, 15, 16, and 17 June 2010, during the first visitor-mode run of observations for our Large Program. The journal of observations and relevant additional information are given in Table 1. The observations comprised 16 separate UVES exposures of ≈4000 s duration taken on five successive nights for a total of ≈64 000 s of integration. Half of the observations were taken with dichroic N. 2 with central wavelengths of the blue and red arms at 437 and 760 nm (setting 437 + 760). The other half were taken with the dichroic N. 1 in the 390 + 580 nm setting. These two wavelength settings overlap somewhat, and as a whole they provide almost complete spectral coverage from 350 up to 947 nm. The CCDs were set with no on-chip binning, and the pixel size ranged between 0.013−0.015 Å pixel^{-1}, or 1.12 km s^{-1}pixel^{-1}at 400 nm, along the dispersion direction. For all observations the slit width was set to 0.8″, providing an instrumental line-spread function with a full width at half maximum (FWHM) of ≈3.57 pixel in the 390 nm frames and ≈4.38 pixel in the 580 nm frame, with a variation of about 20% along the individual echelle orders. This corresponds to a resolving power of $R \approx 55\,000$. During the observations the seeing varied in the range between 0.5″ and 1″ as measured by the Differential Image Motion Monitor telescopes at Paranal Observatory. However, at the slightly higher and more protected location of VLT Unit Telescope 2 (on which UVES is

Table 1. Journal of the observations of HE 2217-2818.

Date	UT	λ_c(nm)	Exp(s)
2010-06-13	05:39:48	390	4000
2010-06-13	06:51:14	390	4000
2010-06-13	08:03:40	390	4000
2010-06-13	09:13:00	390	3600
2010-06-15	05:58:25	390	4000
2010-06-15	07:07:47	390	3767
2010-06-15	08:16:02	390	3767
2010-06-15	09:21:48	390	3767
2010-06-16	05:27:19	437	4020
2010-06-16	06:37:00	437	4020
2010-06-16	07:49:49	437	4000
2010-06-16	08:59:10	437	4020
2010-06-17	05:27:58	437	4000
2010-06-17	06:35:29	437	4000
2010-06-17	07:56:57	437	4000
2010-06-17	09:04:51	437	4000
2010-06-13	05:39:44	580	4000
2010-06-13	06:51:10	580	4000
2010-06-13	08:03:36	580	4000
2010-06-13	09:12:57	580	3600
2010-06-15	05:58:21	580	4000
2010-06-15	07:07:43	580	3767
2010-06-15	08:15:58	580	3767
2010-06-15	09:21:40	580	3767
2010-06-16	05:27:15	760	4020
2010-06-16	06:36:56	760	4020
2010-06-16	07:49:45	760	4000
2010-06-16	08:59:06	760	4020
2010-06-17	05:27:54	760	4000
2010-06-17	06:35:25	760	4000
2010-06-17	07:56:53	760	4000
2010-06-17	09:04:47	760	4000

mounted), the seeing was generally 10−30% better, as measured on the telescope guiding instrumentation.

2.2. Data reduction

We followed two independent approaches to the data reduction. Both analyses utilized the common pipeline language (CPL) version of the various tools constituting the UVES data reduction pipeline[1]. The pipeline first bias-corrects and flat-fields the quasar exposures. The Echelle orders are curved and somewhat tilted with respect to the CCD rows/columns, so the pipeline locates them using an exposure of a quartz lamp observed through a pinhole instead of a standard slit. The quasar flux is then extracted with an optimal extraction method over the several pixels in the cross dispersion direction where the source flux is distributed. The wavelength calibration was performed using ThAr lamp exposures and it is a particularly important step for our purposes − see detailed discussion in Sect. 2.3 below. While the CPL code redisperses the spectra on to a linear wavelength scale by default, we used only the original, un-redispersed flux and error array for each Echelle order in subsequent reduction steps. After wavelength calibration, the air wavelength scale of each quasar exposure was corrected from air to vacuum using the Edlén (1966) formula, and placed in the solar system's barycentric reference frame using the date and time of the mid-point of the exposure's integration.

In the first analysis approach, the extracted flux from individual exposures was redispersed to a common linear wavelength grid and co-added with standard routines within the ESO MIDAS package using the S/N at the Echelle-order centres as weights. The quasar continuum was fitted in local regions around absorption lines with low-order polynomials. In the second analysis approach, a custom code, UVES_POPLER[2] was used to redisperse the flux from individual exposures onto a common log-linear wavelength scale with dispersion 1.3 km s^{-1} pixel^{-1}. The flux from all exposures was scaled to match that of overlapping orders and then co-added with inverse-variance weighting and cosmic ray rejection. UVES_POPLER was also used to automatically fit a continuum to the final spectrum. This continuum was generally acceptable, though some local adjustments were made using low-order polynomial fits in the vicinity of some metal absorption lines.

2.3. Wavelength calibration

A variation in α should manifest itself as small radial velocity shifts between transitions. These transitions may fall many Echelle orders apart in the quasar spectrum. Since the signal for a non-zero $\Delta\alpha/\alpha$ comes from the relative wavelength spacing of these transitions, having an accurate wavelength scale is crucial. The standard method used to calibrate the wavelength scale for a given science exposure with UVES is to take a hollow cathode ThAr arc lamp exposure with the same echelle and cross-disperser settings as the science exposure. Since December 2001, ESO has implemented an automatic resetting of the Cross Disperser encoder positions of UVES at the start of every image acquisition[3]. This policy was introduced to allow the use of day-time ThAr calibration frames to save on night-time calibration overheads. A negative aspect of this choice is that it implies that calibrations are taken under different conditions (e.g. ambient temperature, pressure, telescope pointing, telescope−instrument orientation differences etc.) from those prevailing during the quasar observations. It also implies that a ThAr exposure taken immediately before or after a quasar exposure may not accurately reflect the wavelength scale of the latter: the grating encoders are reset at each new acquisition sequence, so each time the quasar or ThAr arc is acquired for a subsequent exposure, the grating encoders, are, in principle, moved.

One of the principal aims of our new observations is to avoid possible systematic effects introduced by this service calibration plan. Therefore, ThAr exposures were taken before and after each quasar observation during the entire observing run, though only the ThAr frame taken after the quasar exposure was *attached* to the quasar exposure: this special mode allows us to avoid the automatic resets of grating positions between the quasar and calibration exposures. For this reason, the wavelength calibration of each quasar exposure studied in this paper was performed with its corresponding *attached* ThAr exposure. This procedure ensures that no mechanical movements occur between the quasar and ThAr frames and provides the best possible calibration for UVES.

The minimum and maximum temperatures during exposures within the spectrograph in correspondence to the blue arm's CCD camera are monitored. During science exposures, typical changes are $\Delta T \leq 0.1$ K, with two cases showing changes of 0.2 K. Ambient air pressure values are surveyed at the

[1] See http://www.eso.org/observing/dfo/quality/UVES/pipeline/pipe_reduc.html

[2] Written and maintained by MTM http://astronomy.swin.edu.au/~mmurphy/UVES_popler

[3] See the UVES pipeline user manual p. 78.

beginning and end of the exposures and reveal pressure changes of $\Delta P = 0.2$ to 0.8 mbar. The impact of the temperature and pressure variations on UVES radial velocity stability are of 50 m s^{-1} for $\Delta T = 0.3$ K or $\Delta P = 1$ mbar[4]. The measured values assure radial velocity stability within $\approx$50 m s^{-1}. Of course, if such a spurious velocity shift were equally imparted to all transitions in a given spectrum, this would not result in a spurious shift in $\Delta\alpha/\alpha$, because only velocity shifts *between* transitions should affect a measured value of $\Delta\alpha/\alpha$. According to the Edlén (1966) formula for the refractive index of air, pressure, and temperature changes of 0.1 K and 1 mbar would cause *differential* velocity shifts of $\lesssim$15 m s^{-1} across the wavelength range of the spectrum studied here, implying a negligible effect on $\Delta\alpha/\alpha$.

The use of attached ThAr lamps, together with the use of no on-chip pixel binning, and a narrower spectrograph slit are the main differences with respect to most of the previous observations dealing with the search for the variability of fundamental physical constants using UVES.

In the first analysis approach, the wavelength calibration was established with the CPL pipeline's standard method, i.e. extraction of the ThAr flux along the centre of each Echelle order. In the second analysis approach, the ThAr flux was extracted using the object profile weights from its corresponding quasar exposure. The procedure for the selection of ThAr lines and the analysis leading to a wavelength solution follows the one outlined in Murphy et al. (2007a). Specifically, in the 390 nm or 437 nm frames about 400 ThAr lines were identified, and more than 55% of them were used to calibrate the lamp exposures. A polynomial of the fifth order was adopted to match the selected lines. Residuals of the wavelength calibrations were typically $\approx$0.34 mÅ, or $\approx$24 m s^{-1} at 400 nm and symmetrically distributed at all wavelengths. We note that uncertainties of the laboratory wavelengths in individual thorium lines vary from about 15 m s^{-1} up to more than 100 m s^{-1} for the poorly known lines (Lovis & Pepe 2007; Murphy et al. 2007a).

2.4. Slit effects

The optical paths of the ThAr and quasar light beams through the spectrograph are not identical, so there may be effects that cannot be traced by the ThAr calibrations. The most important one is the difference in the slit illumination between a point-like source, such as a quasar, and the calibration lamp, which provides a relatively uniform illumination of the slit. Even when the point-like source is well centred on the slit, the precise position could vary slightly from one exposure to the next, depending also on telescope guiding and tracking. In UVES, a 1.″0 slit-width corresponds to $\approx$7.5 km s^{-1} when projected onto the CCD. Therefore even a small shift of 0.″01 in the centroid of the light is sufficient to induce a shift of $\sim$100 m s^{-1} in the entire spectrum relative to its corresponding ThAr calibration exposure. Exposures taken at different times will in general show different radial velocity shifts due to this effect. Indeed, this effect has been measured by Wendt & Molaro (2012) by cross-correlating 15 UVES spectra of quasar Q0347−383. These spectra showed peak-to-peak excursions of up to $\approx$800 m s^{-1} with an average deviation of 170 m s^{-1}.

Such a slit shift of all metal absorption lines by the same velocity in a single spectrum does not affect $\Delta\alpha/\alpha$. However, this effect becomes relevant when co-adding different exposures and when comparing, as for our observations, spectra obtained with different UVES settings: the mean slit shift will vary as a function of wavelength because of the different contributions from different settings at different wavelengths. This can produce a systematic effect on $\Delta\alpha/\alpha$ if absorption lines from quite different wavelength regions are used. Also, small radial velocity shifts between exposures will produce a slight degradation of the S/N and of the effective instrumental line shape in the final co-added spectrum. The desire to obtain co-added quasar spectra with high S/N precludes the use of individual quasar exposures for analysis because they usually have S/N that are too low. One exception was the very bright quasar HE 0515−4414, which provided one of the highest statistical precisions on $\Delta\alpha/\alpha$ from an individual absorption system so far (Levshakov et al. 2005).

In our first analysis approach we measured the relative slit shifts of the individual quasar exposures by cross-correlating them with the mean spectrum. After selecting regions without telluric lines or cosmic-ray features, we applied the XCSAO code from IRAF to cross-correlating the strongest absorption features. The two settings are summarized in Fig. 1. Despite the fact that relatively few features can be used for the purpose, global radial velocity shifts between different exposures were detected with high confidence. These slit shifts are typically a few hundred m s^{-1} with a maximum amplitude of $\approx$700 m s^{-1}, in agreement with Wendt & Molaro (2012).

The second analysis approach used a custom χ^2 minimization technique to compare each individual exposure with the mean spectrum (rather than a cross-correlation method). This method is described in detail by Evans & Murphy (2013). Its principle advantage for this application is that it does not require prior identification of strong absorption features, instead utilizing all absorption features that contain enough spectral information to provide a reliable shift measurement for each exposure. The slit shifts measured via this second approach are also shown in Fig. 1. In general there is very good agreement between the measurements from the two approaches, broadly consistent with the typical uncertainty of $\sim$30−80 m s^{-1}.

In Fig. 1 it is interesting to note that, in general, the shifts of the two different UVES arms of a given setting are comparable in amplitude and sign. This is expected in the case of good optical alignment of the two separate slits of the two UVES arms (blue and red). This is not obvious a priori because the two arms of the spectrograph have two different entrance slits, and any optical misalignment will produce radial velocity differences between the two arms' spectra. Molaro et al. (2008a) compared the radial velocity measured in the two arms using the sunlight reflected by an asteroid, and came to a similar conclusion. We note that with UVES, no telescope or instrument control is provided to control the relative slit alignment with the desirable accuracy, and the optical alignment can, in principle, change from one observing run to another.

In both analysis approaches, each exposure was corrected for the slit shifts discussed above. The eight exposures were then combined in each setting separately to allow overlapping regions of neighbouring settings to be compared using the same two approaches as are discussed above (cross-correlation and χ^2 minimization). This revealed residual velocity shifts, referred to as "setting shifts" hereafter, between the 390 and 437-nm co-added spectra of -60 ± 52 and -93 ± 38 m s^{-1} in the first and second analysis approaches, respectively. The settings shifts between the overlapping portions of the 580 and 760-nm co-added spectra were -7 ± 48 (first approach) and -155 ± 43 m s^{-1}(second approach). Unfortunately, there are too few strong, particularly narrow absorption features in the small overlapping wavelength range ($\sim$4800−4950 Å) between the 437 and 580-nm settings,

[4] UV-Visual Echelle Spectrograph User Manual, 2004, http://www.eso.org/instruments/uves/userman

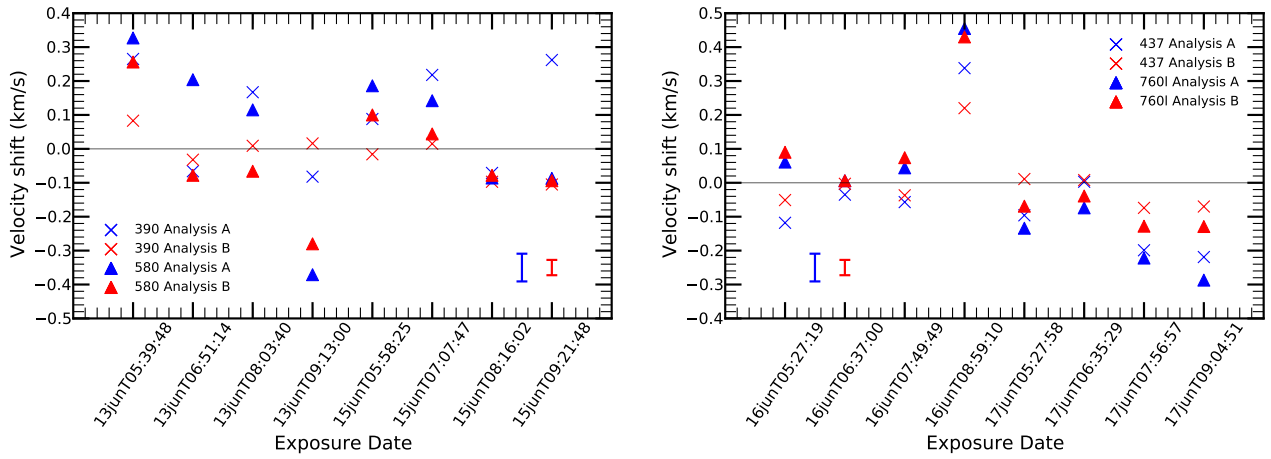

Fig. 1. Radial velocity "slit shifts" between absorption lines in individual exposures and the same lines in the mean spectrum. *Left panel*: shifts for the 390 nm (crosses) and 580 nm (triangles) settings. *Right panel*: shifts for the 437 nm (crosses) and bluer chip of the 760 nm (triangles) settings. In *both panels*, blue points correspond to the first analysis approach and the red points correspond to the second analysis approach. Representative error bars for each analysis approach are shown in each panel.

so we cannot check the setting shifts between them with adequate precision. However, the previous results for the slit shifts between the two UVES arms discussed above provide evidence that the shift between the 437 and 580-nm settings should be consistent with zero within $\sim 30\,\mathrm{m\,s^{-1}}$. That is, we should expect the 390-vs-437-nm and 580-vs-760-nm setting shifts to be consistent with each other within each analysis approach, which we do observe. Indeed, for the second analysis approach, we adopted a single setting shift of $-124 \pm 41\,\mathrm{m\,s^{-1}}$ as representative of the 390-vs-437 and 580-vs-760-nm estimates. We should not expect large differences between the setting shifts of the two different approaches, and this also seems to be observed.

In both analysis approaches, the final spectrum (in which $\Delta\alpha/\alpha$ is to be measured) was formed by co-adding the eight exposures in all settings after removing the "slit shifts" and "setting shifts" from the individual exposures. These final spectra have a high S/N, with values up to ≈100 in the continuum in most of the spectral regions of interest. In Sect. 4.1.1 we consider the effect of not correcting for the slit and setting shifts.

2.5. Known systematic effects in the wavelength calibration

The possible presence of distortions in wavelength scales of Keck/HIRES spectra was investigated by Griest et al. (2010) by comparing the ThAr wavelength scale with the one established from I2-cell observations. In the wavelength range ∼5000−6200 Å covered by the iodine cell absorptions, they found a sawtooth distortion pattern with an amplitude of typically 300 $\mathrm{m\,s^{-1}}$ along each echelle order. The distortions are such that transitions at the order edges appear at different velocities with respect to transitions at the order centres when the two calibrations are compared. Whitmore et al. (2010) repeated the same test for UVES and found similar effects, though the sawtooth distortion shows reduced peak-to-peak velocity variations of $\sim 200\,\mathrm{m\,s^{-1}}$.

The origin of these distortion is not clear. Wilken et al. (2010) detected very small differences in the size of physical pixels due to CCD manufacturing on spectra obtained with the HARPS spectrograph at the 3.6m ESO telescope on La Silla, and calibrated by means of a Laser Frequency Comb. In general, an individual CCD sensor is built up by means of several unit cells or blocks that are connected to each other during the design or layout phase of the development cycle of the sensor. The block stitching process could produce misalignments between different CCD blocks of the order of $\sim 10^{-2}$ of the pixel size. The calibration polynomial cannot cope with these sudden changes in the dispersion solution and oscillates to accommodate it. This overcompensation will produce local calibration distortions. Since blocks have typical sizes of 512 pixels, or ≈13 Å in UVES, shifts could occur even for neighbouring absorption lines, such as the Mg II doublet, or even within a single absorption profile where the components span several hundred $\mathrm{km\,s^{-1}}$ and may fall over two different CCD manufacturing blocks. We test for systematic errors of this kind in Sect. 4.1.1.

We note that Molaro et al. (2011) compared solar features observed both with HARPS and UVES and found such intra-order distortions in the UVES spectrum on a typical scale of ≈10 Å. In HARPS the offsets were measured up to 50 $\mathrm{m\,s^{-1}}$within one order and in UVES, where the pixel size is a factor 3 bigger, the offsets could be a factor 3 larger. We note also that the $\pm 40\,\mathrm{m\,s^{-1}}$ inaccuracies of the HARPS wavelength scale revealed by the Laser Frequency Comb test contribute to the linelist constructed for use with UVES (Lovis & Pepe 2007; Murphy et al. 2007a).

3. Many-multiplet method and fitting

3.1. Many-multiplet method

The change in the rest-frame frequencies between the laboratory, $\omega_i(0)$, and in an absorber at redshift z, $\omega_i(z)$, due to a small variation in α, i.e. $\Delta\alpha/\alpha \ll 1$, is proportional to a q-coefficient for that transition:

$$\omega_i(z) \equiv \omega_i(0) + q_i \left[(\alpha_z/\alpha_0)^2 - 1\right], \quad (1)$$

where α_0 and α_z are the laboratory and absorber values of α, respectively (Dzuba et al. 1999). The q-coefficients for the transitions of interest are given in the last column of Table 2. The change in frequency is observable as a velocity shift, Δv_i, of transition i:

$$\frac{\Delta v_i}{c} \approx -2\frac{\Delta\alpha}{\alpha}\frac{q_i}{\omega_i(0)}. \quad (2)$$

The MM method is based on the comparison of measured velocity shifts from several transitions having different q-coefficients to compute the best-fitting $\Delta\alpha/\alpha$.

When applied across a variety of different ionic species (i.e. different atoms or ionization stages of the same atom), the MM method assumes that the different species trace the same material, or at least that there are no substantial intrinsic velocity shifts between the absorption lines of different species. Therefore, to reduce the number of free parameters in a fit to all transitions of all species, we impose the requirement that corresponding fitted velocity components in different species share the same overall redshifts (i.e. cosmological redshift and peculiar velocity combined). Unless there is evidence that lines are thermally broadened, we also assume that the lines are broadened by macro-turbulence motions. That is, we assume that corresponding velocity components in different species have the same fitted Doppler broadening parameter.

The laboratory atomic parameters used in our analyses – rest-frame frequencies, oscillatory strengths, etc. – were taken from a new compilation (Murphy & Berengut, in prep.), the important details of which are not significantly different from what is used by King et al. (2012). These are reported in Table 2. In particular, the laboratory wavelength for the Fe II λ1608 transition was taken from Nave & Sansonetti (2011). The isotopic structures of most transitions are also reported, together with the composite laboratory wavelength expected for a solar isotope composition.

3.2. Selection of transitions

To build the best model of the velocity structure of an absorption system, we try to include as many different transitions as possible. However, the presence of contaminating absorption lines could strongly skew the analysis, so we did not include transitions that were blended with absorption features of other systems at other redshifts. For the two different analysis approaches, we took two approaches to deal with sky (telluric) lines. The first approach was to remove the regions affected by the telluric lines if their presence could be established based on the spectrum itself, or through comparison with a standard star spectrum taken during our observations. The second approach was more conservative, completely rejecting transitions that had any possible telluric line contamination, even if only in a small part of the velocity structure of the transition. Finally, in neither approach did we consider any transitions that fall in the Lyα forest portion of the spectrum for the analysis of $\Delta\alpha/\alpha$, even if part of their velocity structure presented no evidence of contamination by broad Lyα lines.

3.3. Absorption-line fitting

The model fitting of the absorption profile is performed by means of the non-linear least squares Voigt profile fitting programme VPFIT by Bob Carswell and John Webb[5]. This code has been widely used for the absorption line analysis and has been modified to incorporate α as a free parameter in the fit (Murphy et al. 2003). For a given transition to be fitted, the model is specified by defining the number of components, the spectral region on which the fitting is performed and the instrumental profile. The analysis in both approaches proceeds in two basic steps. The first one consists in obtaining a fiducial model for the absorption

[5] The 9.5 version of the VPFIT manual is available at ftp://ftp.ast.cam.ac.uk/pub/rfc/vpfit9.5.pdf

Table 2. Laboratory atomic data for the transitions used in our analysis, taken from Murphy & Berengut (in prep.; see also King et al. 2012).

Ion	λ_0 [Å]	f or %	q [cm^{-1}]
Mg I 2852	2852.962797(15)	1.83	86(10)
^{26}Mg I 2852	2852.959591(20)	11.0%	
^{25}Mg I 2852	2852.961407(20)	10.0%	
^{24}Mg I 2852	2852.963420(14)	79.0%	
Mg II 2796	2796.353794(16)	0.6155	211(10)
^{26}Mg II 2796	2796.3470457(4)	11%	
^{25}Mg II 2796	2796.348269(50)	4.2%	
^{25}Mg II 2796	2796.352784(50)	5.8%	
^{24}Mg II 2796	2796.3550990(4)	79.0%	
Mg II 2803	2803.530983(16)	0.3058	120(2)
^{26}Mg II 2803	2803.5242094(4)	11%	
^{25}Mg II 2803	2803.525314(50)	4.2%	
^{25}Mg II 2803	2803.530004(50)	5.8%	
^{24}Mg II 2803	2803.5322972(4)	79.0%	
Al II 1670	1670.78861(11)	1.74	270(30)
Al III 1854	1854.717941(34)	0.559	464(30)
$F = 2$	1854.708966(28)	41.7	
$F = 3$	1854.724704(21)	58.3	
Al III 1862	1862.791127(69)	0.278	216(30)
$F = 2$	1862.780325(52)	41.7	
$F = 3$	1862.798581(42)	58.3	
Si II 1526	1526.706980(16)	0.133	50(30)
^{30}Si II 1526	1526.7072550	3.1%	
^{29}Si II 1526	1526.7071150	4.7%	
^{28}Si II 1526	1526.7069637	92.2%	
Fe II 1608	1608.45081(7)*	0.0577	−1299(300)
^{58}Fe II 1608	1608.4519539	0.3%	
^{57}Fe II 1608	1608.4514182	2.1%	
^{56}Fe II 1608	1608.4508635	91.8%	
^{54}Fe II 1608	1608.4496923	5.8%	
Fe II 2344	2344.212747(76)	0.114	1210(150)
^{58}Fe II 2344	2344.2113616	0.3%	
^{57}Fe II 2344	2344.2120103	2.1%	
^{56}Fe II 2344	2344.2126822	91.8%	
^{54}Fe II 2344	2344.2141007	5.8%	
Fe II 2374	2374.460064(78)	0.0313	1590(150)
^{58}Fe II 2374	2374.4582998	0.3%	
^{57}Fe II 2374	2374.4591258	2.1%	
^{56}Fe II 2374	2374.4599813	91.8%	
^{54}Fe II 2374	2374.4617873	5.8%	
Fe II 2382	2382.763995(80)	0.320	1460(150)
^{58}Fe II 2382	2382.7622294	0.3%	
^{57}Fe II 2382	2382.7630560	2.1%	
^{56}Fe II 2382	2382.7639122	91.8%	
^{54}Fe II 2382	2382.7657196	5.8%	
Fe II 2586	2586.649312(87)	0.0691	1490(150)
^{58}Fe II 2586	2586.6475648	0.3%	
^{57}Fe II 2586	2586.6483830	2.1%	
^{56}Fe II 2586	2586.6492304	91.8%	
^{54}Fe II 2586	2586.6510194	5.8%	
Fe II 2600	2600.172114(88)	0.239	1330(150)
^{58}Fe II 2600	2600.1703603	0.3%	
^{57}Fe II 2600	2600.1711816	2.1%	
^{56}Fe II 2600	2600.1720322	91.8%	
^{54}Fe II 2600	2600.1738281	5.8%	

Notes. The third column shows the oscillator strength or, in the case of an isotopic or hyperfine structure component, the terrestrial isotopic abundance fraction or the relative hyperfine level population (in local thermodynamic equilibrium). An asterisk (*) indicates information taken from Nave & Sansonetti (2011).

while keeping $\Delta\alpha/\alpha$ fixed at zero. That is, the number of velocity components and their distribution across the absorption complex is refined without any influence on or from a varying $\Delta\alpha/\alpha$ parameter. Once the model for the absorption has been derived, giving a satisfactory fit of the data with all residuals consistent with the error arrays, $\Delta\alpha/\alpha$ is introduced as a new free parameter to provide a better fit to the data.

The statistical uncertainty in $\Delta\alpha/\alpha$ is determined from the relevant diagonal term of the covariance matrix of the best-fitting solution. This is multiplied by $\sqrt{\chi^2_\nu}$, where χ^2_ν is the χ^2 between the model and data per degree of freedom, ν, to yield more reliable uncertainties (Press et al. 1992). The accuracy and reliability of these statistical uncertainties has been confirmed with detailed Monte Carlo and also Monte-Carlo Markov-chain simulations (King et al. 2009; Murphy 2002). This approach is successful because the covariance between the $\Delta\alpha/\alpha$ parameter and other parameters in the fit is minimal. However, this is not always true for parameters of individual components in the fit. In particular, the column density and Doppler broadening parameters of an individual component are covariant, and strongly covariant with those parameters of close-blended neighbouring components. In the final absorption profile models presented in Tables 4−8, and described in the following sections, we present only statistical uncertainties derived from the diagonal terms of the covariance matrix for the parameters of individual components.

Finally, during the fitting process, we set a lower limit on the Doppler parameter for individual components of $b = 0.5\,\mathrm{km\,s^{-1}}$, which is well below the FWHM resolution of the spectra ($\sim$5.5 $\mathrm{km\,s^{-1}}$). These unresolved components generally have formal uncertainties (quoted in Tables 4−8) exceeding 0.5 $\mathrm{km\,s^{-1}}$. In these cases, and for other components with b-parameters uncertainties exceeding their best-fitted value, it should be recognized that, while b is formally consistent with zero, this does not indicate that the component is redundant in the fit.

3.4. Instrument profile

The FWHM of the instrumental profile of UVES varies by ≈20% along every echelle order due to the spectrograph anamorphosis. Therefore, the FWHM was computed by averaging the width of unblended thorium emission lines in the wavelength region around the metal absorption lines used to derive $\Delta\alpha/\alpha$. That is, the FWHM was calculated separately for each transition. Moreover, it is known that the FWHM of ThAr lines produced by a fully-illuminated slit is slightly broader than what is produced by a point source that under-fills the slit. Simple models suggest that, even with FWHM seeing equivalent to the slit width, the reduction in the FWHM resolution is ≈10%. The values used in the present analysis are those given in Table 3 reduced by 10%.

4. Analysis of absorption systems

We present below the analysis of the five absorption systems towards HE 2217−2818 in which we can measure $\Delta\alpha/\alpha$. We focus first on the highest redshift absorber, the one at $z_{\rm abs} = 1.6919$, because this provides by-far the highest statistical precision on $\Delta\alpha/\alpha$ and, therefore, requires the most comprehensive analysis and consideration of underlying systematic errors. We therefore describe our two different analysis approaches in detail for this system. For the other absorbers, we do not present all details of systematic error checks because the statistical uncertainly dominates the total error budget. We present only the results one analysis approach (the second) for simplicity.

4.1. Absorption system at $z_{\rm abs} = 1.6919$

The system at redshift $z_{\rm abs} = 1.6919$ shows a quite complex velocity structure with many separate strong, narrow features spread over $\sim$250 $\mathrm{km\,s^{-1}}$. The transitions observed redwards of the Lyα forest in our spectral range are potentially useful for measuring $\Delta\alpha/\alpha$ are Al II $\lambda\lambda$1670, Al II $\lambda\lambda$1854, 1862, Mg II $\lambda\lambda$2796 and Fe II $\lambda\lambda$1608, 2344, 2374, 2382, 2586, 2600. Unfortunately, the detected Mg II λ2796 transition cannot be used because it is partially contaminated by a strong sky emission at ≈7526.8 Å. The Mg II λ2803 and Mg I λ2852 transitions were not detected because they fall into the gap between the two red-arm CCDs in the 760-nm setting. The subset of these transitions used to constrain $\Delta\alpha/\alpha$ in the second analysis approach is shown in Fig. 2.

Figure 2 shows that the velocity structure and relative strength of the different features is very similar in all the low-ionization transitions. The Al III $\lambda\lambda$1854/1862 doublet is not observed with high S/N and is not particularly strong. Since a higher ionization species than the other transitions, including it in the analysis may introduce a stronger sensitivity to possible ionization differences between species. However, no evidence of any differences in velocity structure is evident in Fig. 2, even though the relative strength of some features differs from the lower ionization transitions. In general, some features are quite weak even in the stronger transitions and so they are not detectable in the weaker transitions. Even by cursory visual inspection, it is clear that the stronger features are not symmetric and particularly narrow (unresolved); instead, their breadth and asymmetries reveal unresolved complex velocity structure.

Careful inspection of the spectrum of a fast-rotating star allowed us to precisely identify the position of telluric features. The Fe II λ2344, Fe II λ2586, and Fe II λ2600 all fall in a spectral region affected by telluric lines. Removing telluric absorption features is quite a difficult task because they vary with the physical conditions of the Earth's atmosphere, thereby introducing time and line-of-sight dependencies. We did not attempt a correction, but instead we adopted two different approaches to deal with this.

In the first analysis approach we excluded the spectral portions around the telluric lines in these transitions but included the remaining portions in the $\Delta\alpha/\alpha$ analysis. For Fe II λ2344 we considered only the intervals 6310.5−6311.5 and 6312.25−6312.7 Å. For Fe II λ2586 we considered only the intervals 6959.6−6961.5 and 6964.4−6965.75 Å and for Fe II λ2600 the intervals 6996.7−7000.5 and 7001.55−7002.79 Å. Our second analysis approach only considers the transitions that are not affected by telluric or any other contaminating lines. These are the three Fe II transitions $\lambda\lambda$1608, 2374, 2382, the Al II λ1670 transition, and the Al III $\lambda\lambda$1854/1862 doublet, as shown in Fig. 2.

The models of the absorption profiles were built up, step-by-step, by adding components at different velocities in all fitted species simultaneously and minimizing χ^2 at each step with $\Delta\alpha/\alpha$ fixed at zero. The absorber's velocity structure is quite complex, and our first and second analysis approaches used 30 and 32 velocity components, respectively, to obtain statistically acceptable fits with χ^2 per degree of freedom, $\chi^2_\nu \approx 1$. This large number of velocity components is consistent the aforementioned characteristics of the profile: the five main features all show asymmetries and require at least two or three components each to adequately fit them. Additional components are needed to account for weak absorption between these main features and the need for these components is clear from inspecting the line

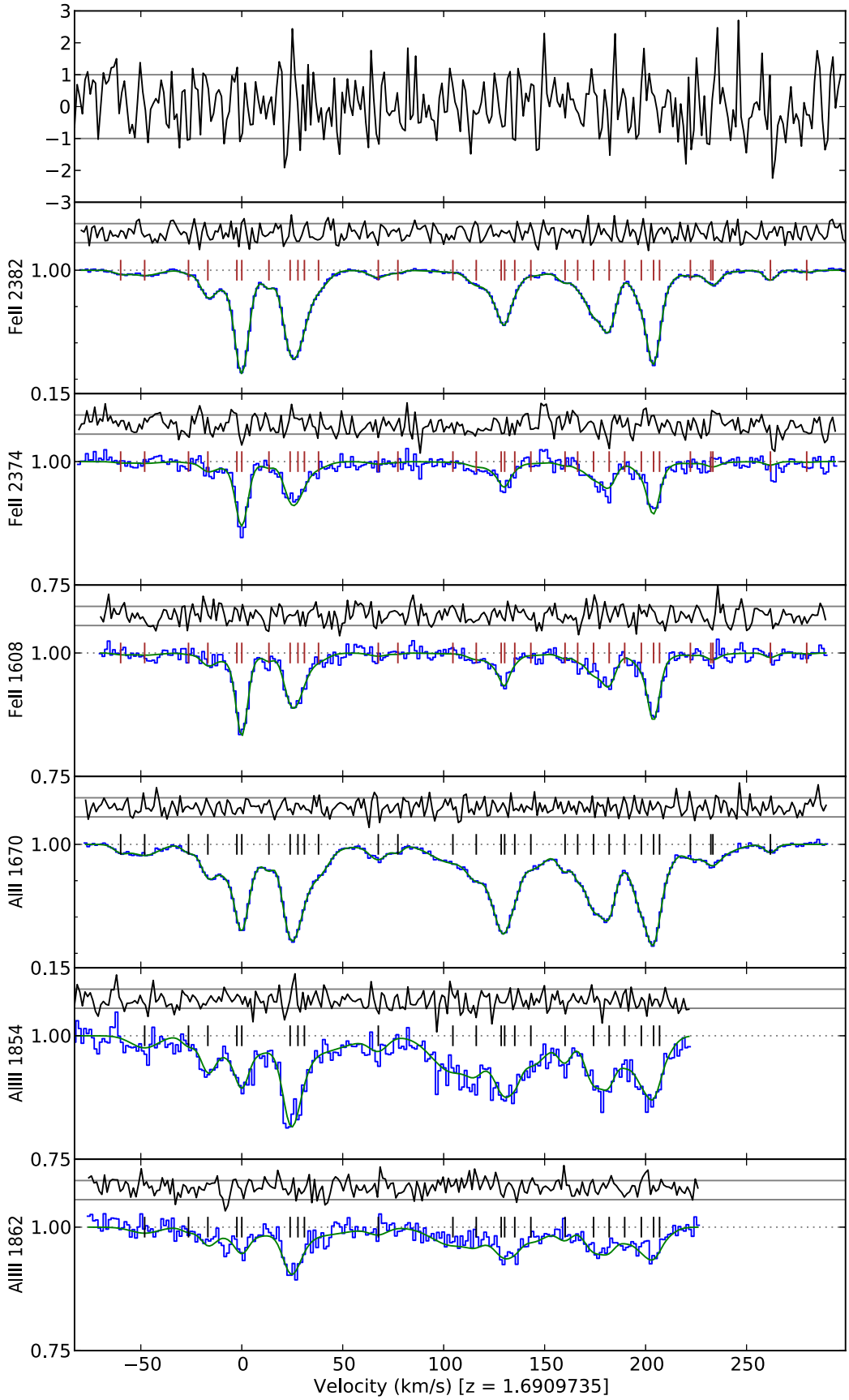

Fig. 2. Transitions in absorption system at $z_{\rm abs}$ = 1.6919 used to derive $\Delta\alpha/\alpha$ in our second analysis approach. The Voigt profile model (green line) is plotted over the data (blue histogram). The velocity of each fitted component is marked with a vertical line, and the residuals between the data and model, normalized by the error spectrum, are shown above each transition. *The top panel* shows the composite residual spectrum − the mean spectrum of the normalized residuals for all transitions shown − in units of σ.

Table 3. Local FWHM of the instrumental profile and local S/N measured in the continuum around each transition for all 5 absorbers studied here.

	z_{abs} = 1.6919		z_{abs} = 1.6279		z_{abs} = 1.5558		z_{abs} = 0.94		z_{abs} = 0.7866	
Ion	*S/N*	*FWHM* [km s^{-1}]	*S/N*	*FWHM* [km s^{-1}]	*S/N*	*FWHM* [km s^{-1}]	*S/N*	*FWHM* [km s^{-1}]	*S/N*	*FWHM* [km s^{-1}]
Fe II 1608	98	5.22								
Fe II 2344	117	5.51	110	5.99	121	5.61				
Fe II 2374	103	5.82								
Fe II 2383	130	5.75	113	5.70	124	5.81	88	5.38	106	5.21
Fe II 2600	88	5.43	84	5.40	84	5.87	71	6.06	73	5.38
Si II 1526	152	5.24	85	5.35	60	5.35				
Al II 1670	77	5.50	78	5.21	100	5.34				
Mg II 2796	78	5.22	96	5.42	97	5.42	53	5.97	65	5.58
Mg II 2803			73	5.42	77	5.42	51	5.95	65	5.58

profiles of the optically thick transitions. We note that these weak components do not influence the value of $\Delta\alpha/\alpha$ significantly. The first analysis approach excluded two of these components; i.e., the first approach represents a "minimally complex" model. Conversely, the second approach required that the chosen model was the one that minimized χ^2_ν. The 32-component model is provided in Table 4, with the final $\chi^2_\nu = 1.20$.

After the number and nominal relative velocities of the fitted components are finalized, $\Delta\alpha/\alpha$ is introduced as an additional free parameter and determined in the χ^2 process along with all other free parameters. The two analysis approaches give the following best-fit values and 1σ statistical uncertainties for $\Delta\alpha/\alpha$:

$$\Delta\alpha/\alpha = \begin{cases} -3.8 \pm 2.1_{\rm stat}\,\text{ppm} & \text{(first approach)}, \\ +1.3 \pm 2.4_{\rm stat}\,\text{ppm} & \text{(second approach)}. \end{cases} \quad (3)$$

The main constraints on $\Delta\alpha/\alpha$ are contributed by the combination of the high S/N transitions with diverse q-coefficients, i.e. those of Al II and Fe II, particularly the Fe II λ1608 transition, that has a q-coefficient with an opposite sign to the others. The results from the two analysis approaches in Eq. (3) appear at first to be rather inconsistent. This may indicate that important systematic errors are present in the calibration and analysis steps, since these constitute the main difference between the two approaches. We explore possible systematic errors in more detail in Sect. 4.1.1 below.

One notable difference between the two analysis approaches is that the first includes six Fe II transitions, or parts thereof (after masking telluric features), thereby making an analysis that uses just those transitions feasible. Using just one ionic species alleviates the possibility that ionization effects may systematically affect $\Delta\alpha/\alpha$ (e.g. Levshakov et al. 2005). Of course, in the case of Fe II, the precision and accuracy of the result depend heavily on the Fe II λ1608 transition, and any possible systematic errors applying to the data or wavelength calibration relevant to it. To conduct this Fe-only test, we restricted the region analysed in each transition to the velocity range −35 to +250 km s^{-1} in Fig. 2. This effectively removed the two velocity components in the model for the first approach that corresponds to the weak features at the blue and red flanks of the absorber. A further two velocity components from that model were discarded as unnecessary by VPFIT because the high S/N Al II λ1670 transition had been removed. This left the model with 26 components. Furthermore, we derived $\Delta\alpha/\alpha$ on a different reduction of the spectrum, with a slightly different binning and exposure combination approach to those presented above. The result based on this Fe-only analysis is $\Delta\alpha/\alpha = +1.14 \pm 2.58_{\rm stat}$ ppm. The difference between this result and the one from the first approach in Eq. (3) demonstrates that systematic effects may play an important role in the total uncertainty in $\Delta\alpha/\alpha$. We turn to quantifying the systematic error budget for this absorber below.

4.1.1. Systematic error tests

We ran a number of tests on the second analysis approach to uncover the sensitivity of the result to various systematic effects. For each of these tests, we find the maximum deviation between the second approach's $\Delta\alpha/\alpha$ value in Eq. (3) and the one given by the test, adding the results in quadrature to estimate the total systematic error budget.

Firstly, to test the convergence of the fitting procedure, we restarted the χ^2 minimization from its final solution but with starting values of $\Delta\alpha/\alpha$ set to $+1\sigma$ and -1σ away from its fiducial value. Both these test fits converged to $\Delta\alpha/\alpha$ values very close to those in Eq. (3). The largest difference was 0.03 ppm, which we added in quadrature to the total systematic error budget.

The second test investigated the effect that co-adding the individual exposures into a final spectrum has on the absorption line centroids and, therefore, $\Delta\alpha/\alpha$. The software used to combine the spectra in the second analysis approach, UVES_POPLER, first redisperses all Echelle orders, from all exposures, onto a common wavelength scale with a constant pixel size in velocity space. A dispersion of 1.30 km s^{-1} pixel^{-1} was used for the final spectrum. To test the effect of redispersing and co-adding the individual exposures, we produced four new co-added spectra with slightly different dispersion values – 1.28, 1.29, 1.3, and 1.32 km s^{-1} pixel^{-1} , which ensures that the pixel grids will be very different for each transition from spectrum to spectrum. The values of $\Delta\alpha/\alpha$ for these four different spectra varied by at most 0.54 ppm, and this was added in quadrature to the total systematic error budget.

The third test quantified the possible effect the intra-order distortions of the UVES wavelength scale found by Whitmore et al. (2010) may have on $\Delta\alpha/\alpha$. For each Echelle order, of each exposure, we applied a sawtooth distortion to the existing wavelength scale and then co-added them in the usual way. The distortion applied had a peak-to-peak amplitude of 200 m s^{-1}, varying from −100 m s^{-1} at the order edges to +100 m s^{-1} and the order centres. We also produced a second distorted spectrum where this sawtooth pattern was reversed. Of course, we cannot be sure that the effect identified by Whitmore et al. (2010) is present in our spectra or that it has the same pattern or magnitude in our spectra, but the two distorted spectra produced in this way allow us to gauge the size of the effect on $\Delta\alpha/\alpha$. Refitting for $\Delta\alpha/\alpha$ on

these distorted spectra gives a maximum deviation between the distorted and fiducial results of 0.56 ppm.

The final test was aimed at understanding the effect that the slit shifts and setting shifts discussed in Sect. 2.4 have on $\Delta\alpha/\alpha$. The most straightforward test is to determine $\Delta\alpha/\alpha$ using spectra in which these corrections have *not* been applied in the second analysis approach. Unsurprisingly, not applying the setting shift ($-124 \pm 41\,\mathrm{m\,s^{-1}}$) produces the largest difference in $\Delta\alpha/\alpha$, 1.2 ppm, thus demonstrating that, were these effects not corrected, they would have caused a significant systematic error, or about 50% of the statistical error. However, while we have corrected for these effects, we can not have done so perfectly, and errors in our corrections will propagate as systematic errors in $\Delta\alpha/\alpha$. The relative uncertainty on the setting shift is 33%, so we expect that the residual systematic error in this case is of the order of 0.4 ppm.

After adding the above estimates of the systematic error in quadrature, the total systematic error budget is 0.96 ppm. That is, the final result from the second analysis approach is

$$\Delta\alpha/\alpha = +1.3 \pm 2.4_{\mathrm{stat}} \pm 1.0_{\mathrm{sys}}\,\mathrm{ppm}\,. \quad (4)$$

4.2. Absorption system at $z_{\mathrm{abs}} = 1.6279$

The transitions used to constrain $\Delta\alpha/\alpha$ in the second analysis approach for the absorption system at $z_{\mathrm{abs}} = 1.6279$ are shown in Fig. 3. The absorption profile model parameters from this approach are provided in Table 5. The absorption spans $\sim$100 km s^{-1} with three main features that are rather broad and very asymmetric, revealing quite a complex underlying velocity structure. Detected transitions not used to constrain $\Delta\alpha/\alpha$ include strong Si II λ1526 absorption, which falls in the Lyα forest.

The broad and multi-component nature of the three main absorption features translates to large statistical uncertainties on the redshifts of the velocity components and, therefore, to $\Delta\alpha/\alpha$. The systematic error budget was determined by conducting the same systematic error tests as conducted on the $z_{\mathrm{abs}} = 1.6919$ absorber in Sect. 4.1.1. The final result for this $z_{\mathrm{abs}} = 1.6279$ absorber is then

$$\Delta\alpha/\alpha = +37.2 \pm 20.6_{\mathrm{stat}} \pm 39.4_{\mathrm{sys}}\,\mathrm{ppm}. \quad (5)$$

4.3. Absorption system at $z_{\mathrm{abs}} = 1.5558$

The transitions used to constrain $\Delta\alpha/\alpha$ in the second analysis approach for the absorption system at $z_{\mathrm{abs}} = 1.5558$ are shown in Fig. 4. The absorption profile model parameters from this approach are provided in Table 6. The absorption spans $\sim$100 km s^{-1} with three main features that appear at first to be rather symmetric and narrower than the three features in the $z_{\mathrm{abs}} = 1.6279$ absorber. Indeed, the underlying velocity structure of these three features appears to be dominated by a single strong component in each case. However, our detailed approach to fitting all the *statistically required* velocity components reveals that several weaker components are required for an adequate fit. These are required for the higher optical depth transitions of Mg II λ2796 and Al II λ1670. There are three telluric features that contaminate the Mg II λ2803, so this is excluded from the analysis.

The χ^2 minimization analysis of the $z_{\mathrm{abs}} = 1.5558$ profiles shown in Fig. 4 and the systematic error tests conducted in Sect. 4.1.1 provide a final result of

$$\Delta\alpha/\alpha = -0.2 \pm 24.9_{\mathrm{stat}} \pm 3.6_{\mathrm{sys}}\,\mathrm{ppm}. \quad (6)$$

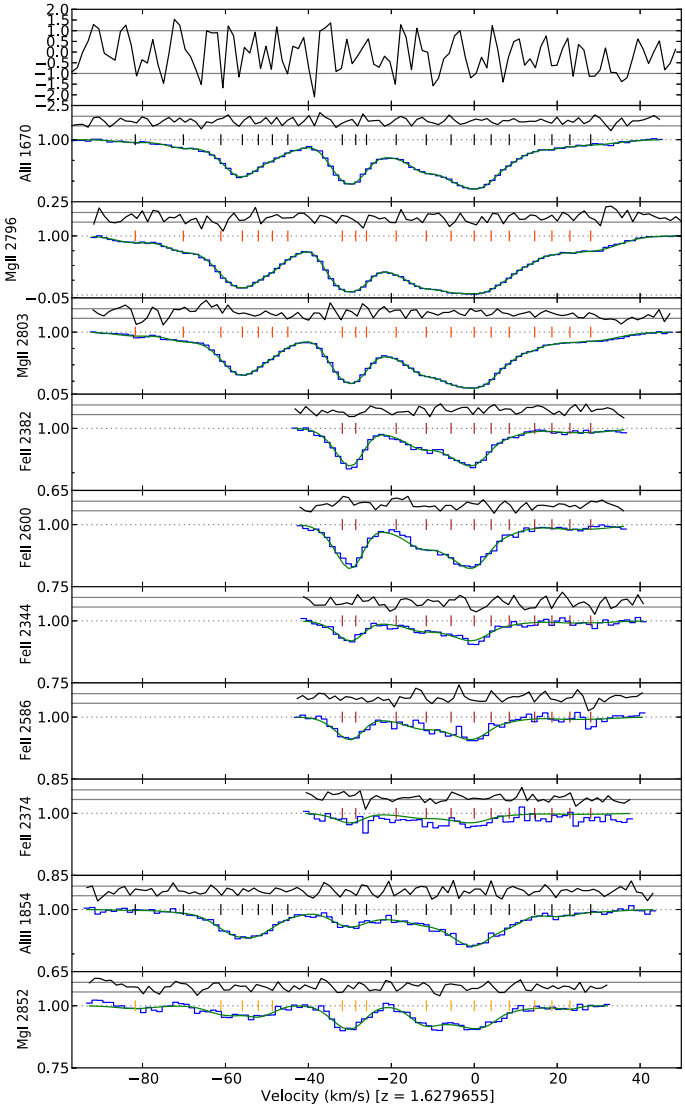

Fig. 3. Absorption profile for system at $z_{\mathrm{abs}} = 1.6279$ with transitions used in the second analysis approach for determining $\Delta\alpha/\alpha$. The figure is structured as in Fig. 2. Details of the absorption profile fit are given in Table 5.

Given the relatively large statistical uncertainty on $\Delta\alpha/\alpha$ in this absorber, we neglect here the systematic error budget because it will be much smaller.

4.4. Absorption systems at $z_{\mathrm{abs}} = 0.9407$ and 0.9424

The absorption around $z_{\mathrm{abs}} = 0.941$ comprises two absorption complexes, one with the main absorption at $z_{\mathrm{abs}} = 0.9407$ and the second with the strongest absorption at $z_{\mathrm{abs}} = 0.9424$. They are separated by $\sim$300 km s^{-1} without any hint of absorption in any of the strongest detected transitions. We therefore fit them separately. The transitions used to constrain $\Delta\alpha/\alpha$ in the second analysis approach for these systems are shown in Figs. 5 and 6. The absorption profile model parameters from this approach are provided in Table 7.

The absorption at $z_{\mathrm{abs}} = 0.9407$ spans $\sim$100 km s^{-1} and at $z_{\mathrm{abs}} = 0.9407$ it spans $\sim$180 km s^{-1} in the strongest transition, Mg II λ2796. The first system comprises two well-separated features, while the second comprises four closely separated strong features, but in both systems the strong features are broad and

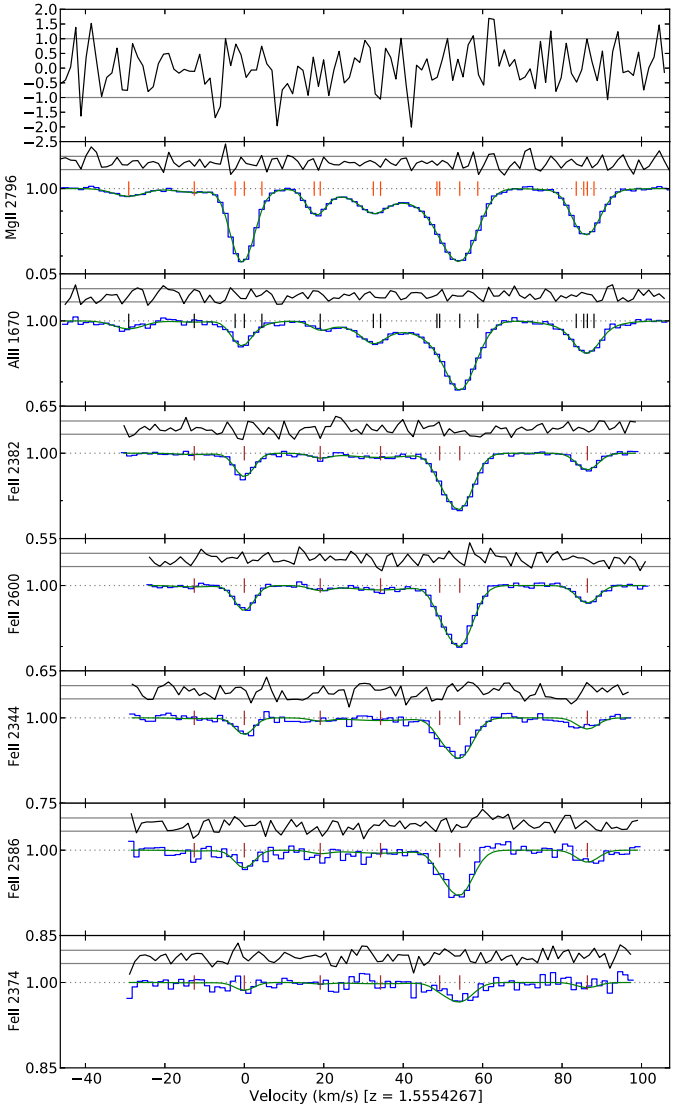

Fig. 4. Absorption profile for system at $z_{\rm abs}$ = 1.5558 with transitions used in the second analysis approach for determining $\Delta\alpha/\alpha$. The figure is structured as in Fig. 2. Details of the absorption profile fit are given in Table 6.

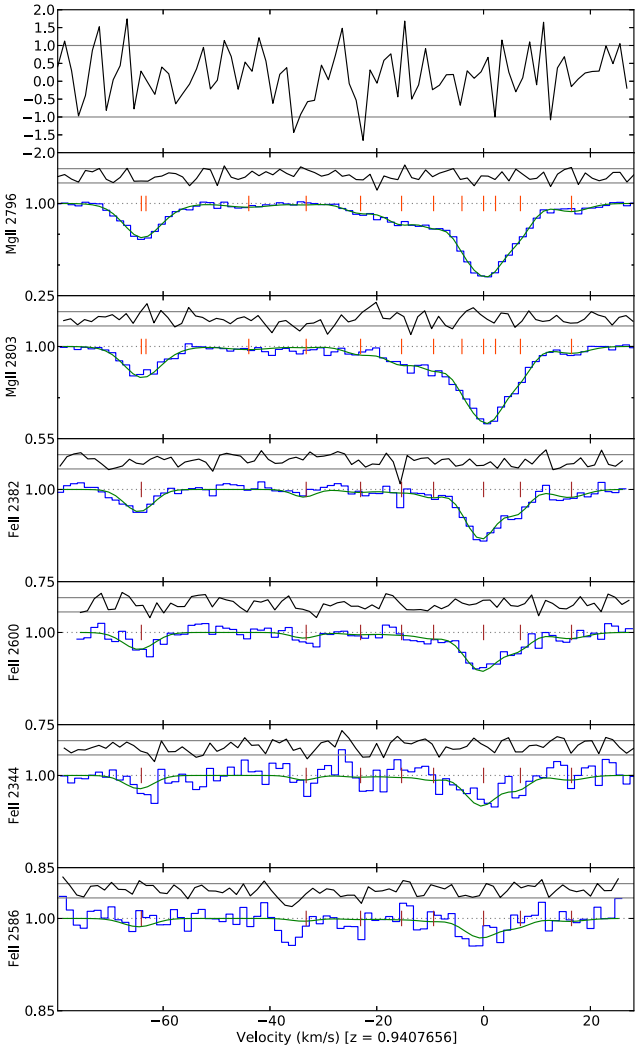

Fig. 5. Absorption profile for system at $z_{\rm abs}$ = 0.9407 with transitions used in the second analysis approach for determining $\Delta\alpha/\alpha$. The figure is structured as in Fig. 2. Details of the absorption profile fit are given in Table 7.

smooth with strong asymmetries. Thus, fairly complex absorption models were fitted to these systems, with the strong features comprising several velocity components of similar strength each.

The χ^2 minimization analysis of the profiles shown in Figs. 5 and 6, and the systematic error tests in Sect. 4.1.1, provide the following results:

$$\Delta\alpha/\alpha = \begin{cases} +21.4 \pm 24.2_{\rm stat} \pm 20.9_{\rm sys} \ \text{ppm} & \text{at } z_{\rm abs} = 0.9407, \\ +9.3 \pm 12.7_{\rm stat} \pm 9.8_{\rm sys} \ \text{ppm} & \text{at } z_{\rm abs} = 0.9424. \end{cases} \quad (7)$$

Given the relatively large statistical uncertainties on $\Delta\alpha/\alpha$ in these absorbers, we neglect the systematic error budgets because they will be much smaller.

4.5. Absorption system at $z_{\rm abs}$ = 0.7866

The transitions used to constrain $\Delta\alpha/\alpha$ in the second analysis approach for the absorption system at $z_{\rm abs}$ = 0.7866 are shown in Fig. 7. The absorption profile model parameters from this approach are provided in Table 8. The absorption spans ∼90 km s^{-1} in one broad complex of several highly blended features, each of which shows visual evidence of asymmetries, and none of which are particularly narrow. Thus, like all the other absorbers studied here, the main absorption features require several velocity components for an adequate fit. Detected transitions not used to constrain $\Delta\alpha/\alpha$ include strong Si II λ1526 absorption that falls in the Lyα forest.

The χ^2 minimization analysis of the $z_{\rm abs}$ = 0.7866 profiles shown in Fig. 7 and the systematic error tests in Sect. 4.1.1 provide a final result of

$$\Delta\alpha/\alpha = +7.3 \pm 35.9_{\rm stat} \pm 21.4_{\rm sys} \ \text{ppm}\,. \quad (8)$$

Given the relatively large statistical uncertainty on $\Delta\alpha/\alpha$ in this absorber, we neglect here the systematic error budget because it will be much smaller.

5. Discussion

Current searches for cosmological variations in the fine-structure constant are based on the analysis of large samples of absorption

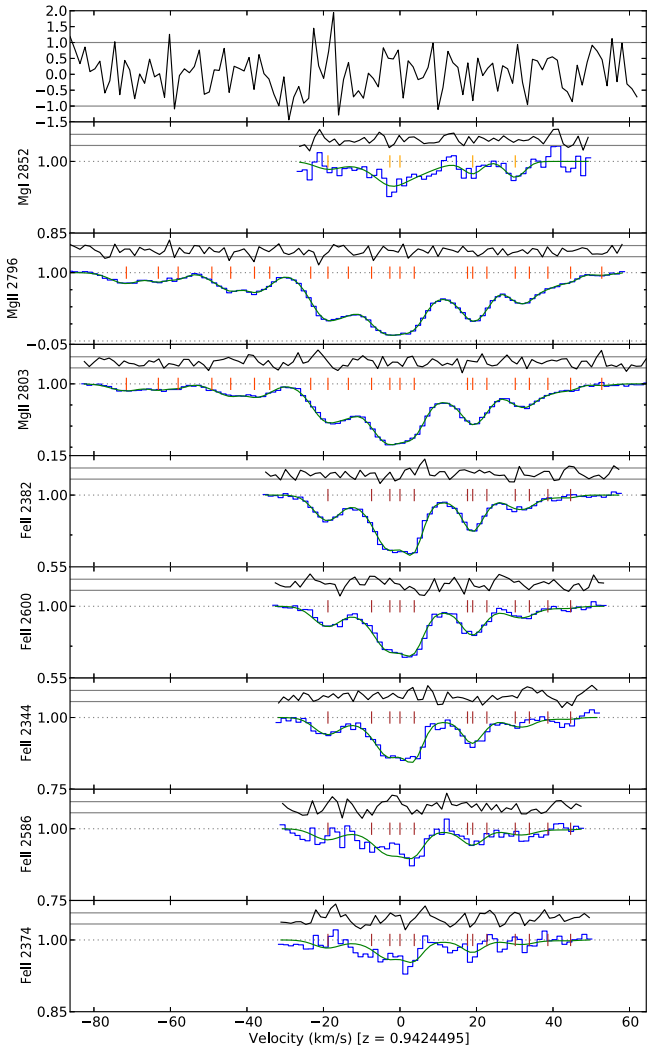

Fig. 6. Absorption profile for system at $z_{\rm abs}$ = 0.9424 with transitions used in the second analysis approach for determining $\Delta\alpha/\alpha$. The figure is structured as in Fig. 2. Details of the absorption profile fit are given in Table 7.

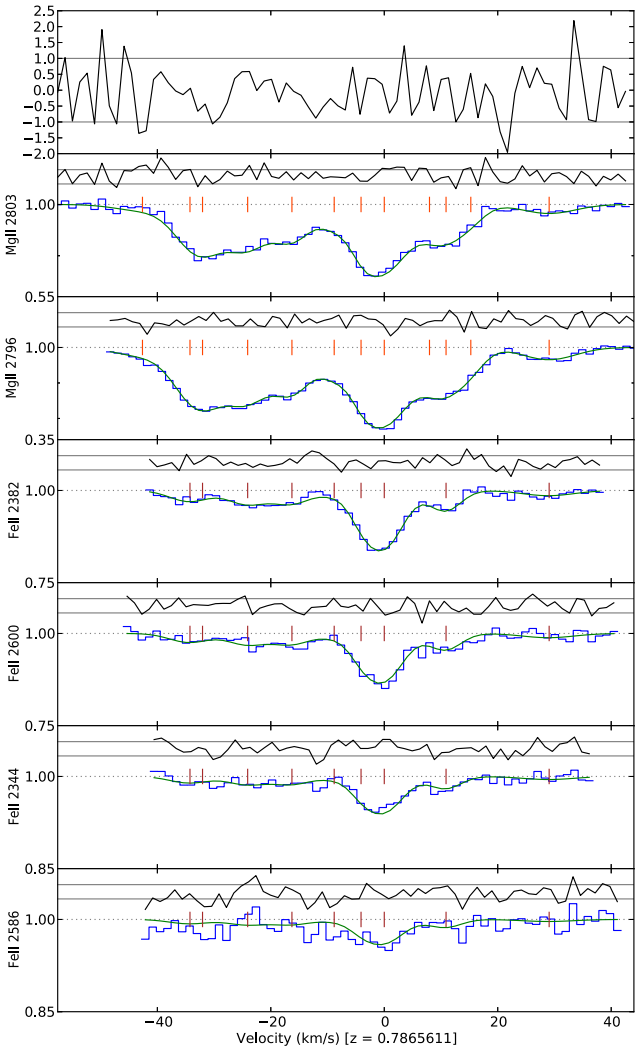

Fig. 7. Absorption profile for system at $z_{\rm abs}$ = 0.7866 with transitions used in the second analysis approach for determining $\Delta\alpha/\alpha$. The figure is structured as in Fig. 2. Details of the absorption profile fit are given in Table 8.

systems observed at different redshifts and directions in the sky. Thanks to the large size of these samples, it is possible to reach an ensemble sensitivity of a few ppm in $\Delta\alpha/\alpha$. On the other hand, deep observations of a few selected lines of sight are capable of producing measurements with similar statistical errors. The two approaches have both intrinsic merits: the former is more effective in detecting possible changes as a function of redshift or across different regions of space, and possibly for averaging down systematic effects; the last allows more detailed analysis, potentially facilitating the identification of possible systematic errors that may go undetected in a large number of systems.

The line of sight towards the relatively bright quasar HE 2217−2818 is rich with absorption systems. Our MM analysis of the five systems observed at $z_{\rm abs}$ = 0.7866, 0.9407, 0.9424, 1.5558, 1.6279 and 1.6919 provides no evidence of a change of the fine-structure constant. In particular, the system at $z_{\rm abs}$ = 1.6919 provides a very precise bound on variations in α: $\Delta\alpha/\alpha = +1.3 \pm 2.4_{\rm stat} \pm 1.0_{\rm sys}$ ppm. This result, stemming from our second analysis approach in which we conducted several tests to constrain the systematic error budget, differs somewhat from the first approach, conducted separately with different details of the data reduction, calibration, and analysis: $\Delta\alpha/\alpha$ =-3.8 ± $2.1_{\rm stat}$ ppm. This may indicate that systematic errors are greater than expected from the range of tests we conducted. However, it is interesting to note that restricting the first approach to the six Fe II transitions and using a modified absorption model yields a similar result to the second approach, $\Delta\alpha/\alpha = +1.1 \pm 2.6_{\rm stat}$ ppm. Clearly, it is important to continue to refine the analysis techniques to minimize differences in the results obtained by different approaches. Our future papers on this and other quasars in our Large Program of new VLT/UVES observations will aim at that goal.

The main reasons for the small statistical uncertainty in $\Delta\alpha/\alpha$ from the $z_{\rm abs}$ = 1.6919 absorber are the several narrow absorption features across its absorption profile including the Fe II λ1608 transition that, compared to the other Fe II transitions in particular, provide a wide range of q-coefficients among the fitted transitions, and the high S/N of the spectra. Unfortunately, the absorption features that characterize the four other absorbers tended to be somewhat broader. And with a narrower range of q coefficients available from the fitted transitions, the statistical uncertainties in those absorbers exceeded 10 ppm.

The bound on $\Delta\alpha/\alpha$ obtained from the $z_{\rm abs}$ = 1.6919 system is one of the most precise measurements available from an

Table 9. Summary of $\Delta\alpha/\alpha$ results including 1σ statistical uncertainties and estimated systematic errors for the 5 absorption systems towards HE 2217−2818 studied here.

z	$\Delta\alpha/\alpha$ [ppm]	$\sigma_{\rm stat}$ [ppm]	$\sigma_{\rm sys}$ [ppm]	χ^2_ν	Ions
0.7866	+7.32	35.89	21.36	1.29	Fe II, Mg II
0.9407	+21.40	24.16	20.86	1.13	Fe II, Mg II
0.9424	+9.32	12.68	9.84	1.30	Fe II, Mg II
1.5558	-0.15	24.90	3.55	1.21	Fe II, Al II, Si II, Mg II
1.6279	+37.22	20.62	39.44	1.43	Fe II, Al II, Si II, Mg II, I
1.6919 (A)	-3.84	2.10		0.96	Fe II, Al II
1.6919 (A)	+1.14	2.58		0.94	Fe II
1.6919 (B)	+1.29	2.35	0.96	1.19	Fe II, Al II, III

Notes. Our two separate analysis results for the absorber at $z_{\rm abs} = 1.6919$ are identified in parentheses.Our two separate analysis results for the absorber at $z_{\rm abs}$=1.6919 are identified in parentheses.

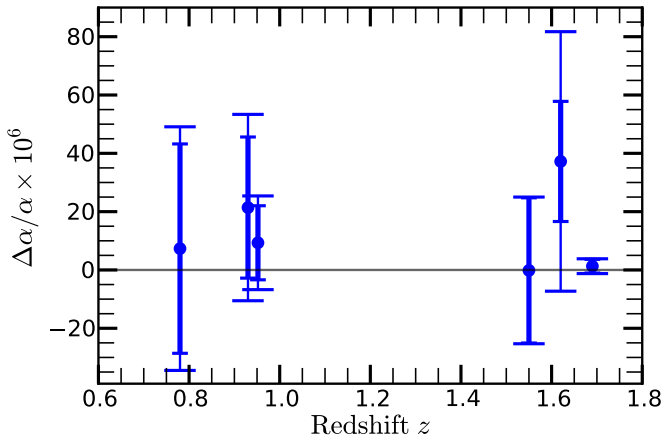

Fig. 8. Summary of $\Delta\alpha/\alpha$ measurements towards HE 2217−2818. Each absorption system's $\Delta\alpha/\alpha$ value from the second analysis approach is plotted with its 1σ statistical uncertainty, plus the total uncertainty formed by quadrature addition of the statistical and systematic errors in Table 9.

individual absorber. Three other studies of individual absorbers have claimed measurements with comparably small uncertainties. These are $\Delta\alpha/\alpha = -0.07 \pm 1.8$ ppm obtained from absorption at $z_{\rm abs} = 1.15$ towards the extremely bright quasar HE 0515−4414 (Molaro et al. 2008b), $\Delta\alpha/\alpha = 5.4 \pm 2.5$ ppm from the system at $z_{\rm abs} = 1.84$ towards quasar Q 1101−264 (Levshakov et al. 2006), and $\Delta\alpha/\alpha = -1.5 \pm 2.6$ ppm from the system at $z_{\rm abs} = 1.58$ towards HE 0001−2340 (Agafonova et al. 2011). The first two were both obtained by comparing only Fe II lines with each other, while the last was derived through a comparison of Fe II and Si II transitions. The result at $z_{\rm abs} = 1.6919$ presented here was obtained by comparing Al II λ1670 and several Fe II transitions, including Fe II λ1608. Broad agreement is found when using only the Fe II lines, particularly when considering the total systematic error budget of 2.4 ppm and the strong dependence on Fe II λ1608 in that case. Therefore, we find no strong evidence of any influence from differential ionization effects that may be present when comparing different ions.

Recently, King et al. (2012) have analysed a new sample of 153 measurements obtained from observations taken with UVES at the ESO VLT, adding to the previous sample of 143 absorption systems obtained from the analysis of Keck/HIRES spectra (Murphy et al. 2003). The two samples generally probe different directions in the universe, and rather surprisingly they show a different dependence on redshift; that is, α has appeared on average to be smaller in the past in the northern hemisphere but larger in the past in the southern hemisphere. This is particularly the case for the combined dataset at redshift $\geq$1.8. Overall, the variation across the sky can be simply and consistently represented by a monopole (i.e. a constant offset in α from the current laboratory value) plus a spatial dipole in the direction with right ascension 17.3 ± 1.0 h and declination −61 ± 10 degrees (King et al. 2012). The spatial dependence is fitted with $\Delta\alpha/\alpha = m + A\cos\Theta$, where A is the dipole amplitude $A = 9.7 \pm 2.1$ ppm, Θ is the angle on the sky between a quasar sight-line and the best-fit dipole position, and $m = -1.78 \pm 0.84$ ppm is the monopole term. A simpler model, without the monopole term, gives $A = 10.2 \pm 2.1$ ppm with a pole towards right ascension 17.4 ± 0.9 h and declination −58 ± 9 degrees (King et al. 2012).

The dipole amplitude of ≈10 ppm could in principle be revealed by precise measurements along individual lines of sight. The pole and anti-pole directions are observationally difficult regions to study, particularly the pole that is very close to the Galactic centre and virtually devoid of bright quasars. Towards the directions for which precise individual absorbers have been studied, the variation in α expected by the dipole model is small and cannot be revealed by current accuracies[6]. However, the line of sight towards HE 2217−2818 subtends an angle $\Theta = 58.8°$ with respect to the simple dipole-only model above which it is small enough to produce a signal that may be detectable along this single line of sight: the predicted signal is $\Delta\alpha/\alpha = +5.4 \pm 1.7$ ppm. For a simple comparison with our main result here ($\Delta\alpha/\alpha = +1.3 \pm 2.4_{\rm stat} \pm 1.0_{\rm sys}$ ppm), we combined its statistical and systematic error terms in quadrature, which reveals that it differs from this simple dipole prediction (including its uncertainty) by 1.3σ. The prediction from the monopole+dipole model at the sky position of HE 2217−2818 is $\Delta\alpha/\alpha = +3.2 \pm 1.7$ ppm[7]. Thus, our most precise result towards HE 2217−2818 does not directly support evidence of a dipolar variation in α across the sky, though it does not provide compelling evidence against it either.

6. Conclusions

The line of sight towards the relatively bright quasar HE 2217−2818 is rich with absorption systems and is located in the sky at a favourable position for probing the recently proposed presence of spatial variation of the fine structure constant, α. It is the first quasar from our ongoing VLT/UVES Large Program to measure $\Delta\alpha/\alpha$ in ∼25 absorbers towards ∼12 bright quasars, from which we expect to make ∼20 measurements of $\Delta\alpha/\alpha$ with precision $\lesssim$10 ppm. Approximately ten of these – the absorbers that are the main targets of the Large Programme – will provide very high statistical precisions of ∼2 ppm each and systematic uncertainties $\lesssim$2 ppm. This will yield a final ensemble precision of better than 1 ppm with the additional aim of better understanding possible systematic uncertainties at this accuracy level.

[6] The simple dipole model used here predicts the following values of $\Delta\alpha/\alpha$ for the three quasars with previous precise measurements: 2.6 ± 1.4 ppm (HE 0001−2340), 2.2 ± 1.6 ppm (HE 0515−4414), and 3.5 ± 1.4 (Q 1101−264).

[7] A simple PYTHON programme by J.B.W. for estimating the predicted dipole can be found at http://pypi.python.org/pypi/dipole_error/.

Our MM analysis here of the five absorption systems observed at $z_{abs} = 0.7866, 0.9407, 0.9424, 1.5558, 1.6279$ and 1.6919 is in keeping with these goals: the highest-redshift absorber provides a very precise and robust measurement at the ∼2 ppm level while the four others provide weaker constraints ≳10 ppm.

The high S/N, sharp absorption features, and diversity of sensitivity to α in the transitions of the $z_{abs} = 1.6919$ absorber provides the most stringent measurement of $\Delta\alpha/\alpha$ for this line of sight. Two separate approaches to the data reduction, calibration, and absorption-line fitting yielded slightly different results $-\ \Delta\alpha/\alpha = -3.8 \pm 2.1_{stat}$ ppm and $\Delta\alpha/\alpha = +1.3 \pm 2.4_{stat}$, though both are consistent with no variation in α. We also investigated a number of sources of systematic errors in this system and the effect that they might have on the final measurement. Our final result for this absorber, including both statistical and systematic error terms, is $\Delta\alpha/\alpha = +1.3 \pm 2.4_{stat} \pm 1.0_{sys}$. The results for all the absorption systems are summarized in Table 9.

If the evidence for a spatial variation of α across the sky presented by Webb et al. (2011) and King et al. (2012) represents reality, then the simplest model of those results − a dipolar variation in α − predicts $\Delta\alpha/\alpha = 5.4 \pm 1.7$ ppm in the direction of the line of sight of HE 2217−2818. Our constraint on $\Delta\alpha/\alpha$ from the $z_{abs} = 1.6919$ absorber neither strongly supports nor conflicts with that prediction.

Acknowledgements. An anonymous referee is acknowledged for several pieces of advice. P.M. and C.J.M. acknowledge support from grants PTDC/FIS/111725/2009 and PTDC/CTE-AST/098604/2008 from the FCT, Portugal. The work of P.M. was partially funded by grant CAUP-06/2010-BCC. The work of C.J.M. is funded by a Ciência 2007 Research Contract, funded by FCT/MCTES (Portugal) and POPH/FSE (EC). M.T.M. thanks the Australian Research Council for funding under the *Discovery Projects* scheme (DP110100866). P.P.J. is supported in part by Agence Nationale pour la Recherche under contract ANR-10-Blan-0510-01. R.S. and P.P.J. gratefully acknowledge support from the Indo-French Centre for the Promotion of Advanced Research (Centre Franco-Indien pour la promotion de la recherche avancée) under Project N.4304-2. S.L. has been supported by FONDECYT grant number 1100214. The work of I.I.A. and S.A.L. is supported by DFG Sonderforschungsbereich SFB 676 Teilprojekt C4 and, in part, by the State Programme Leading Scientific Schools of Russian Federation (grant NSh 4035.2012.2).

References

Agafonova, I. I., Molaro, P., Levshakov, S. A., & Hou, J. L. 2011, A&A, 529, A28
Amendola, L., Leite, A. C. O., Martins, C. J. A. P., et al. 2012 Phys. Rev. D, 86, 3515
Bahcall, J. N., Sargent, W. L. W., & Schmidt, M. 1967, ApJ, 149, L11
Chand, H., Srianand, R., Petitjean, P., & Aracil, B. 2004, A&A, 417, 853
Dzuba, V. A., Flambaum, V. V., & Webb, J. K. 1999, Phys. Rev. Lett., 82, 888
Edlén, B. 1966, Metrologia, 2, 71
Evans, T. M., & Murphy, M. T. 2013, ApJ, submitted
Griest, K., Whitmore, J. B., Wolfe, A. M., et al. 2010, ApJ, 708, 158
King, J. A., Mortlock, D. J., Webb, J. K., & Murphy, M. T. 2009, Mem. Soc. Astron. It., 80, 864
King, J. A., Webb, J. K., Murphy, M. T., et al. 2012, MNRAS, 422, 3370
Levshakov, S. A., Centurión, M., Molaro, P., & D'Odorico, S. 2005, A&A, 434, 827
Levshakov, S. A., Centurión, M., Molaro, P., & Kostina, M. V. 2006, A&A, 447, L21
Lovis, C., & Pepe, F. 2007, A&A, 468, 1115
Molaro, P., Levshakov, S. A., Monai, S., et al. 2008a, A&A, 481, 559
Molaro, P., Reimers, D., Agafonova, I. I., & Levshakov, S. A. 2008b, EPJ Spec. Topics, 163, 173
Molaro, P., Centurión, M., Monai, S., & Levshakov, S. 2011, Spectrographs, Asteroids and Constants, eds. C. Martins, & P. Molaro, Astrophysics and Space Science Proc. (Berlin Heidelberg: Springer-Verlag), 167
Murphy, M. T. 2002, Probing variations in the fundamental constants with quasar absorption lines, Ph.D. Thesis, University of New South Wales
Murphy, M. T., Webb, J. K., Flambaum, V. V., et al. 2001, MNRAS, 327, 1208
Murphy, M. T., Webb, J. K., & Flambaum, V. V. 2003, MNRAS, 345, 609
Murphy, M. T., Udem, T., Holzwarth, R., et al. 2007a, MNRAS, 380, 839
Murphy, M. T., Webb, J. K., & Flambaum, V. V. 2007b, Phys. Rev. Lett., 99, 239001
Murphy, M. T., Webb, J. K., & Flambaum, V. V. 2008, MNRAS, 384, 1053
Nave, G., & Sansonetti, C. J. 2011, J. Opt. Soc. Am. B, 28, 737
Olive, K. A., Peloso, M., & Uzan, J.-P. 2011, Phys. Rev. D, 83, 3509
Press, W. H., Teukolsky, S. A., Vetterling, W. T., & Flannery, B. P. 1992, Numerical recipes in C. The art of scientific computing (Cambridge University Press)
Quast, R., Reimers, D., & Levshakov, S. A. 2004, A&A, 415, L7
Savedoff, M. P. 1956, Nature, 178, 688
Srianand, R., Chand, H., Petitjean, P., & Aracil, B. 2007, Phys. Rev. Lett., 99, 9002
Webb, J. K., Flambaum, V. V., Churchill, C. W., Drinkwater, M. J., & Barrow, J. D. 1999, Phys. Rev. Lett., 82, 884
Webb, J. K., King, J. A., Murphy, M. T., et al. 2011, Phys. Rev. Lett., 107, 1101
Wendt, M., & Molaro, P. 2012, A&A, 541, A69
Whitmore, J. B., Murphy, M. T., & Griest, K. 2010, ApJ, 723, 89
Wilken, T., Lovis, C., Manescau, A., et al. 2010, MNRAS, 405, L16

Pages 15 to 17 are available in the electronic edition of the journal at http://www.aanda.org

Table 4. Multi-component Voigt profile model and χ^2 minimization results for the absorber at $z_{\rm abs} = 1.6919$.

z	σ_z	b [km s^{-1}]	σ_b [km s^{-1}]	log N(Fe II) [cm^{-2}]	σ_N [cm^{-2}]	log N(Al II) [cm^{-2}]	σ_N [cm^{-2}]	log N(Al III) [cm^{-2}]	σ_N [cm^{-2}]
1.6904350	0.0000070	3.7	1.4	10.99	0.18				
1.6905417	0.0000087	9.0	1.4	11.50	0.07	11.24	0.06	11.19	0.10
1.6907366	0.0000068	3.1	1.4	10.92	0.16	10.72	0.11	10.77	0.20
1.6908227	0.0000019	3.8	0.6	11.87	0.08	11.33	0.12	11.33	0.09
1.6909516	0.0000071	11.7	1.9	12.27	0.04	11.93	0.04	11.56	0.13
1.6909735	0.0000005	2.6	0.1	12.67	0.01	11.78	0.03	11.21	0.11
1.6910942	0.0000022	1.2	1.1	11.46	0.07	10.93	0.09		
1.6911884	0.0000037	4.1	0.6	12.34	0.44	11.92	0.28	11.62	0.22
1.6912232	0.0000218	5.6	1.3	12.51	0.31	11.84	0.35	11.38	0.39
1.6912519	0.0000317	25.5	6.5	10.90	0.99	11.45	0.14	11.82	0.08
1.6913146	0.0000079	6.0	0.9	11.87	0.11	11.46	0.10		
1.6915804	0.0000036	5.3	0.8	11.45	0.05	11.17	0.05	11.04	0.15
1.6916675	0.0000059	1.7	1.8	10.75	0.18	10.60	0.13		
1.6919120	0.0000159	13.8	1.8	11.18	0.15	11.65	0.07	11.85	0.07
1.6920159	0.0000080	5.2	1.0	11.71	0.11	11.45	0.15	11.24	0.22
1.6921268	0.0000167	6.0	1.8	12.27	0.20	12.08	0.20	11.63	0.23
1.6921421	0.0000025	0.5	0.3	11.83	0.14	11.24	0.39	10.50	0.68
1.6921871	0.0000155	2.4	3.4	11.27	1.24	11.11	1.10	11.05	0.55
1.6922586	0.0000231	10.4	3.4	11.59	0.19	11.67	0.16	11.64	0.16
1.6924106	0.0000037	3.7	0.8	11.57	0.07	11.33	0.09	11.22	0.10
1.6924667	0.0000040	0.5	2.0	11.30	0.17	11.14	0.58		
1.6925374	0.0000061	5.3	1.1	12.29	0.09	11.92	0.09	11.61	0.09
1.6926068	0.0000029	3.6	0.5	12.31	0.08	11.82	0.11	11.43	0.14
1.6926757	0.0000106	3.4	2.5	11.12	0.52	11.07	0.36	11.19	0.22
1.6927497	0.0000095	4.7	1.1	12.04	0.30	11.84	0.25	11.50	0.32
1.6928042	0.0000010	2.6	0.3	12.54	0.10	11.89	0.18	11.22	0.46
1.6928307	0.0000648	6.7	4.8	12.01	0.65	11.69	0.62	11.44	0.60
1.6929678	0.0000116	4.0	3.3	11.09	0.37	10.76	0.53		
1.6930588	0.0000248	12.3	2.4	11.45	0.22	11.47	0.13		
1.6930679	0.0000026	3.1	0.9	11.52	0.10	10.77	0.22		
1.6933236	0.0000021	2.7	0.5	11.42	0.03	10.73	0.06		
1.6934849	0.0000126	4.0	2.5	10.82	0.15				

$\Delta\alpha/\alpha$ [ppm]	$\sigma_{\rm stat}$ [ppm]	χ^2_ν
+1.29	2.35	1.19

Notes. The redshift (z), Doppler broadening parameter (b), and relevant column densities for each velocity component are presented, along with their 1σ uncertainties from VPFIT, are provided in the main section of the table. The fitted value for $\Delta\alpha/\alpha$, its 1σ statistical uncertainty (see text for systematic error component) and the final χ^2 per degree of freedom, χ^2_ν, are provided in the lower part.

Table 5. As in Table 4 but for the absorption system at $z_{abs} = 1.6279$.

z	σ_z	b [km s^{-1}]	σ_b [km s^{-1}]	log N(Al II) [cm^{-2}]	σ_N [cm^{-2}]	log N(Al III) [cm^{-2}]	σ_N [cm^{-2}]	log N(Mg II) [cm^{-2}]	σ_N [cm^{-2}]	log N(Mg I) [cm^{-2}]	σ_N [cm^{-2}]	log N(Fe II) [cm^{-2}]	σ_N [cm^{-2}]
1.6272489	0.0000071	5.7	0.9	10.69	0.10	10.30	0.47	11.48	0.07	9.96	0.20		
1.6273505	0.0000094	4.9	1.3	11.13	0.14	10.79	0.26	11.81	0.15				
1.6274298	0.0000342	4.3	3.1	11.26	0.71	11.36	0.57	12.04	0.71	10.28	0.47		
1.6274753	0.0000080	3.8	1.5	11.76	0.27	11.61	0.40	12.54	0.27	10.19	0.74		
1.6275091	0.0000076	0.5	1.0	10.84	0.55	11.14	0.25	11.77	0.36	10.02	0.28		
1.6275388	0.0000048	1.0	0.7	10.97	0.34	11.01	0.28	11.80	0.25	9.88	0.27		
1.6275714	0.0000215	5.0	3.1	11.29	0.30	11.21	0.30	11.98	0.30				
1.6276866	0.0000333	4.0	1.7	11.74	1.00	11.33	1.30	12.54	0.93	10.61	0.64	11.52	0.63
1.6277150	0.0000071	2.9	0.6	11.45	0.65	10.87	2.08	12.37	0.40	10.38	0.75	11.83	0.30
1.6277377	0.0001969	4.9	18.5	11.34	3.06	11.15	3.07	12.05	3.07	9.57	3.04		
1.6278005	0.0000141	4.3	1.8	11.29	0.26	11.15	0.26	12.15	0.21			11.17	0.24
1.6278641	0.0000061	4.3	1.0	11.74	0.12	11.45	0.14	12.61	0.13	10.74	0.09	11.72	0.12
1.6279165	0.0000063	2.5	1.2	11.48	0.46	11.28	0.49	12.42	0.39	10.22	0.56	11.40	0.53
1.6279655	0.0000083	4.0	2.3	11.97	0.25	11.85	0.23	12.83	0.25	10.74	0.25	11.98	0.23
1.6280013	0.0000079	1.2	2.0	11.11	0.74	10.54	1.92	11.91	0.85	9.96	0.69	10.86	1.35
1.6280395	0.0000153	3.7	2.4	11.53	0.29	11.49	0.27	12.29	0.31	10.13	0.37	11.31	0.34
1.6280932	0.0000041	0.7	0.5	10.78	0.22	10.36	0.60	11.72	0.14	9.33	0.69	10.42	0.41
1.6281297	0.0000036	0.8	0.6	10.82	0.06	10.80	0.16	11.51	0.07	9.42	0.55	10.27	0.36
1.6281677	0.0000054	0.5	1.7	10.36	0.17	10.61	0.25	11.11	0.14	9.73	0.25	10.24	0.42
1.6282117	0.0000062	8.2	0.6	11.12	0.06	10.93	0.17	12.00	0.04			11.24	0.08

$\Delta\alpha/\alpha$ [ppm]	σ_{stat} [ppm]	χ^2_ν
+37.22	20.62	1.43

Table 6. As in Table 4 but for the absorption system at $z_{abs} = 1.5558$.

z	σ_z	b [km s^{-1}]	σ_b [km s^{-1}]	log N(Mg II) [cm^{-2}]	σ_N [cm^{-2}]	log N(Al II) [cm^{-2}]	σ_N [cm^{-2}]	log N(Fe II) [cm^{-2}]	σ_N [cm^{-2}]
1.5551786	0.0000039	4.4	0.7	11.28	0.05			10.61	0.18
1.5553193	0.0000162	5.2	2.1	11.01	0.12	10.55	0.66	9.83	1.69
1.5554070	0.0000120	0.5	1.0	12.44	1.93			10.46	0.44
1.5554267	0.0000046	1.3	0.4	13.04	0.78	11.63	0.02	10.77	0.31
1.5554644	0.0000496	2.8	7.8	10.86	1.14			10.09	1.26
1.5555767	0.0000074	0.5	3.1	11.63	0.78				
1.5555896	0.0000052	1.4	1.8	11.24	0.59	10.85	0.24	10.38	0.30
1.5557036	0.0000026	2.1	1.1	11.37	0.16			10.60	0.22
1.5557190	0.0000094	10.7	2.5	11.89	0.08	11.34	0.08	11.12	0.09
1.5558400	0.0000474	4.9	3.3	11.83	0.65			10.99	0.65
1.5558459	0.0000062	0.5	1.0	11.13	0.72	11.36	0.21	9.88	2.07
1.5558890	0.0000050	3.4	0.3	12.47	0.15	12.16	0.03	11.47	0.21
1.5559277	0.0000161	3.0	1.4	11.45	0.38			10.81	0.30
1.5561390	0.0000372	1.1	4.6	11.55	1.35			10.27	1.38
1.5561551	0.0000132	8.3	2.6	11.15	0.49			10.93	0.22
1.5561629	0.0000047	2.1	0.4	11.74	8.58	11.49	0.03	10.75	5.19
1.5561771	0.0003294	2.4	16.0	11.58	11.21			10.39	10.88

$\Delta\alpha/\alpha$ [ppm]	σ_{stat} [ppm]	χ^2_ν
−0.15	24.90	1.21

Table 7. As in Table 4 but for the absorption systems at $z_{abs} = 0.9407$ and $z_{abs} = 0.9424$.

z	σ_z	b [km s^{-1}]	σ_b [km s^{-1}]	log N(Mg II) [cm^{-2}]	σ_N [cm^{-2}]	log N(Fe II) [cm^{-2}]	σ_N [cm^{-2}]	log N(Mg I) [cm^{-2}]	σ_N [cm^{-2}]
0.9419861	0.0000024	4.5	0.7	11.58	0.03				
0.9420403	0.0000037	0.5	1.1	11.28	0.13				
0.9420738	0.0000039	0.5	1.7	11.16	0.15				
0.9421309	0.0000122	0.5	3.2	11.07	0.44				
0.9421628	0.0000051	2.0	3.3	11.66	0.25				
0.9422031	0.0000095	1.7	3.6	11.65	0.33				
0.9422289	0.0000151	0.5	2.2	11.25	0.58				
0.9422983	0.0000761	4.9	9.3	11.40	1.40				
0.9423275	0.0000031	3.8	0.6	12.35	0.17	11.86	0.07	9.99	0.23
0.9423621	0.0000040	0.5	0.5	11.73	0.15				
0.9424014	0.0000491	5.1	8.8	12.14	0.92	11.53	0.92		
0.9424324	0.0000039	3.3	1.0	12.44	0.45	12.08	0.27	9.96	0.65
0.9424495	0.0000130	9.6	2.8	12.48	0.28	11.83	0.44	10.70	0.13
0.9424737	0.0000027	1.8	0.6	12.28	0.14	12.06	0.10		
0.9425639	0.0000308	6.7	4.3	12.19	0.40	11.53	0.47		
0.9425727	0.0000032	1.5	1.0	12.04	0.27	11.79	0.15	10.04	0.17
0.9425967	0.0000107	1.6	3.6	11.62	0.80	11.01	0.80		
0.9426448	0.0000048	1.9	1.7	11.81	0.26	11.36	0.21	10.19	0.13
0.9426687	0.0000053	0.5	0.7	11.79	0.18	11.18	0.23		
0.9427000	0.0000077	2.6	3.8	11.60	0.30	10.84	0.41		
0.9427385	0.0000069	0.5	1.2	11.28	0.22	10.62	0.27		
0.9427913	0.0000064	2.1	2.9	10.77	0.14				
$\Delta\alpha/\alpha$ [ppm]	σ_{stat} [ppm]	χ^2_ν							
+9.32	12.7	1.30							
0.9403508	0.0000033	2.5	0.8	11.48	0.33	11.33	0.05		
0.9403564	0.0000052	5.0	1.6	11.55	0.27				
0.9404810	0.0000098	4.9	3.0	10.85	0.14				
0.9405506	0.0000068	0.5	7.4	10.16	0.46	10.76	0.20		
0.9406165	0.0000102	2.3	2.7	11.11	0.23	10.42	0.36		
0.9406662	0.0000043	2.4	2.7	11.47	0.17	10.49	0.39		
0.9407050	0.0000057	0.5	0.6	11.50	0.11	10.76	0.15		
0.9407394	0.0000195	1.0	3.6	11.50	0.83				
0.9407656	0.0000033	3.0	0.6	12.07	0.73	11.73	0.03		
0.9407801	0.0000229	1.2	5.0	11.65	1.35				
0.9408103	0.0000033	0.9	0.8	11.63	0.07	11.24	0.08		
0.9408722	0.0000038	3.0	1.3	11.07	0.07	10.91	0.12		
$\Delta\alpha/\alpha$ [ppm]	σ_{stat} [ppm]	χ^2_ν							
+21.40	24.2	1.13							

Table 8. As in Table 4 but for the absorption system at $z_{abs} = 0.7866$.

z	σ_z	b [km s^{-1}]	σ_b [km s^{-1}]	log N(Mg II) [cm^{-2}]	σ_N [cm^{-2}]	log N(Fe II) [cm^{-2}]	σ_N [cm^{-2}]
0.7863071	0.0000787	5.8	10.8	11.20	1.23		
0.7863570	0.0000483	3.7	5.5	11.21	10.38	11.11	2.40
0.7863702	0.0000753	4.6	2.7	12.04	1.53	8.98	380.73
0.7864176	0.0000086	3.4	4.3	11.90	0.58	11.19	0.55
0.7864641	0.0000091	3.5	2.9	11.87	0.30	11.18	0.30
0.7865085	0.0000065	1.2	2.2	11.44	0.17	10.52	0.47
0.7865367	0.0000047	0.5	0.8	11.75	0.24	11.09	0.61
0.7865611	0.0000067	3.7	1.2	12.14	0.18	11.85	0.12
0.7866086	0.0001375	5.0	22.5	11.81	2.81		
0.7866260	0.0000052	2.3	1.0	11.46	3.37	11.29	0.06
0.7866520	0.0000245	1.8	8.5	11.31	3.32		
0.7867343	0.0000040	5.6	1.1	11.36	0.05	10.90	0.11
$\Delta\alpha/\alpha$ [ppm]	σ_{stat} [ppm]	χ^2_ν					
+7.32	35.89	1.29					